# Multiscale Topology Optimization of modulated fluid microchannels based on asymptotic homogenization

Florian Feppon

# MULTISCALE TOPOLOGY OPTIMIZATION OF MODULATED FLUID MICROCHANNELS BASED ON ASYMPTOTIC HOMOGENIZATION

F. FEPPON[1]

[1] *NUMA Unit, Department of Computer Science, KU Leuven, Belgium.*

Abstract. Dehomogenization techniques are becoming increasingly popular for enhancing lattice designs of compliant mechanical systems with ultra-large resolutions. Their effectiveness hinges on computing a deformed periodic grid that enable to reconstruct fine-scale designs with modulated and oriented patterns. In this paper, we propose an approach for extending dehomogenization methods to laminar fluid systems. We initiate our methodology by asymptotically deriving Darcy's law on a periodically porous medium deformed by a diffeomorphism. Unlike the mechanical context, we reveal that the homogenized permeability matrix depends not solely on local the orientation but also on the local dilation of the deformed periodic medium. This distinction presents one of the several challenges to be tackled when adapting dehomogenization-based topology optimization techniques to porous media. To accommodate existing methodologies, we formulate a simplified "poor man's" homogenized model, which streamlines various aspects, yet still leans on periodic cell problems to estimate the spatially varying permeability matrix. Specifically, we overlook boundary layer effects, we presume periodic grid deformations, and we neglect local dilation, solely considering the relationship with local cell orientations. Subsequently, we present a numerical approach for designing a system that redistributes an input flow across numerous regularly spaced outlets at an output interface. Leveraging the homogenized model, we deduce optimized geometric arrangements of local channel spacing parameters and orientations. We then use established methods to reconstruct grid deformations and fine-scale designs. The fidelity of these reconstructions is then validated through fine-scale simulations. Our observations indicate that while the proposed designs yield satisfactory performance when subjected to the full-scale model, discernible deviations from the homogenized model persist, appealing to future improvements.

**Keywords.** Mulsticale Topology Optimization, homogenization, porous media, spatially modulated locally periodic medium, Darcy's law.

**AMS Subject classifications.** 35B27, 65K10, 65N99, 35Q93

---

Contents



---

* Corresponding author. Email: florian.feppon@kuleuven.be. The author declares having no conflict of interest with respect to the publication of the content of this article. .

## 1. Introduction

Topology Optimization (TO) has revolutionized industrial design processes by automating the creation of optimized physical systems [13, 8]. The rise of additive manufacturing has expanded the scope of feasible designs [28], making TO increasingly popular in industries like automotive where it's used to design lightweight supporting components. Among these increased capabilities, additive manufacturing is opening the way towards achieving ultra-fine resolutions in printing structures, potentially down to the nanometer level [61]. However, traditional TO methods struggle when it comes to capturing the intricate microscopic details needed for multiscale designs due to the need for highly detailed and computationally intensive meshes.

To address these limitations, the field of multiscale Topology Optimization has emerged, see [64] for a review. The goal of multiscale TO is to create designs that optimize both the overall shape and the microscopic lattice-like structures To achieve this in reasonable computational time, multiscale TO takes advantage of homogenization theory [51, 7], which predicts how materials will behave on a larger scale by averaging out the tiny details on a smaller scale. With the benefit of rigorous asymptotic analysis, the effective medium can be conceptualized as a homogeneous entity possessing smooth, homogenized material attributes. These attributes are explicitly derived by solving a cell problem within a representative periodic unit cell. This makes it possible to simulate the physics of the medium using coarse meshes, reducing drastically the computational effort compared to running full simulations with ultra-fine grids.

A promising subclass of multiscale Topology Optimization are *dehomogenization methods* [41, 9, 37]. These methods generate optimized designs with geometrically modulated periodic patterns in a two-steps process. In the initial step, an optimal microstructure is computed. This microstructure is characterized by a concise set of smoothly changing geometric parameters and the local orientation of the periodic cell. Subsequently, in the second step, a distorted grid is deduced from the optimized orientation. This grid manipulation allows for projecting the finely tuned geometric parameters onto a viable design spanning various length scales. The deformed grid is numerically described by a diffeomorphism, which is the key ingredient for successfully generating periodically modulated lattice structures with spatially oriented cells.

The microstructure parameters are optimized on a coarse mesh, while the final reconstruction of the multiscale design on a fine mesh is relatively inexpensive. As a result, dehomogenization enables to generate large-scale, high-resolution multiscale structures without the computational burden that classical Topology Optimization would demand on exceptionally fine mesh.

So far, multiscale TO methods, including dehomogenization techniques, have been primarily applied to the design of mechanical structures. However, there is a great potential for their application to the design of systems featuring complex arrangements of fluid channels, such as microfluidic devices and heat exchangers. Microfluidic devices in particular are commonly used in various applications from biology, chemistry [57, 12], for instance for DNA separation [29]. They require careful design of fluid channels to meet requirements such as uniform output pressure through multiple outlets [49, 26, 45, 63]. Recent advancements in additive manufacturing have made it possible to produce micro-architectured designs, which have shown to improve performance and efficiency [55, 60].

The development of multiscale TO methods for fluid systems is fairly recent and has been the object of only a few publications; none of them using dehomogenization based methods whereby the locally periodic microstructure is projected on a deformed grid. The first work investigating optimal porous media can be found in [44], where classical TO was used to determine the geometry of periodic microstructures maximizing the components of the Darcy–permeability tensor. This approach was still not coupled to a macroscale model. The first truly multiscale TO method for fluid systems was developed in the PhD thesis [65] for the design of micropillar arrays constituting a microfluidic device. The author relied on a Brinkman model with a penalization factor parameterized by the local volume fraction according to an empirical constitutive law. After optimizing the local volume fraction, micropillars arrays were subsequently reconstructed and aligned according to the fluid strain tensor directions.

Subsequently, Dede and his co-authors published a number of works using a reaction-diffusion equation to generate Turing patterns, which effectively dehomogenize optimized porous designs into microchannel flows. In their initial work, [26] utilized an empirical analytical Darcy model relating fluid channel widths to the inverse permeability. This approach was expanded in [27], where the permeability coefficient was numerically estimated by solving an empirical cell problem, and dehomogenized designs were successfully experimentally validated. In these two works, fluid microchannels were reconstructed according to the macroscopic fluid streamlines. Then, the authors considered a different modelling approach for optimizing convection-reaction systems in [68, 45], where the orientation of the channels was considered as the key design variable.

The optimization of multiscale fluid-thermal devices was considered in [52] by resorting to the Brinkman model and to a homogenized convection-diffusion equation derived by physical modelling. The optimized designs include "gray regions" corresponding to porous parts of the design which were not dehomogenized. More

recently, [53, 54] proposed a multiscale TO method for the optimization of the orientations and sizes of micropillars that could be selected among a set of predefined shapes relying on a Stokes model penalized with the Darcy permability matrix obtained by periodic homogenization. Finally, [19] developed a multiscale Topology Optimization method relying on recent macroscale models obtained by the volume averaging technique, still observing large discrepancies with direct fluid simulations.

As these references suggest, one of the major challenges to address when devising dehomogenization methods for fluid systems comes from the multiplicity of available homogenized models relating the geometry of the porous microstructure to the macroscale fluid behavior, not all of them being mathematically justified. In fact, extending dehomogenization methods to fluid systems pose serious difficulties that are not present in the context of mechanical systems.

First, *scaling effects* come into play: the mathematical literature on homogenization of porous media states that different homogenized models apply to different scaling regimes between the size of the periodic inclusions and the distance between them [58, 4, 31]. Assuming that the solid obstacles are distributed on the cells of a grid with periodicity $\epsilon$, the physics of the porous medium is described by the Darcy equation. Still, if the solid obstacles become tiny, with size of the order of $\epsilon^3$ (in three dimensions), the physics of the medium is then described by the Brinkman model [3]. Solid inclusions of size much smaller than $\epsilon^3$ have no effects; the physics of the medium is then that of the Navier-Stokes equation. In order to apply gradient based optimization methods to multiscale design of fluid systems, there is a need for effective model that would account for pure fluid to pure solid regions and all possible transitions between the Brinkman and Darcy regimes; the derivation of homogenized equations accurate at higher order powers in $\epsilon$ can represent a possible research direction towards the derivation of such ideal models [36].

Second, classical homogenization theory still only applies to academic systems with *idealized boundaries and periodic microstructures*, while realistic multiscale systems features inlets and outlets as well as spatially varying microstructures. Boundary conditions in heterogeneous media create boundary layers which impact the homogenized field inside the domain which are known to be quite delicate to describe analytically [5, 14, 38, 50].

A third difficulty, that we discuss in Section 3, comes from the fact that the Darcy permeability tensor on a deformed periodic domain depends on the local stretching experienced by the distorted medium. This is a major difference with the setting of linear elasticity where this effect does not exist for the homogenized stiffness matrix. For instance, diminishing the size of the periodic cell within a composite elastic material by a factor of 2 doesn't alter its effective properties. However, in the context of a porous material, reducing the radius and the relative spacing of periodic solid obstacles by a factor of two results in a fourfold increase in the permeability tensor. The invariance of the effective properties by rescaling is a rather strong assumption of previous dehomogenization based multiscale methods [41, 9], which would need to be addressed when developing future dehomogenization based methods for fluid systems.

In this paper, we develop a "poor man's approach" to dehomogenization based Topology Optimization of fluid microchannels that ignore these three difficulties. The intention of the paper is to provide a proof of concept of the applicability of the dehomogenization techniques previously developed for mechanical structures to the context of fluid channels. We rely on multiple simplifying assumptions such as ignoring boundary layers, scaling regimes and the dependence of the permeability matrix to the local dilation. Still, as an important methodological difference with respect to the dehomogenization methods of [26, 68, 27, 45], we rely on asymptotic homogenization to compute the macroscopic permeability tensor from the geometry of the microstructure rather than empirical numerical or analytical permeability models. The advantage of using asymptotic homogenization for computing the permeability matrix lies in the fact that it potentially leads to mathematically justified approximations (up to the limitations exposed above). The use of analytical or numerical empirical models does not require an online precomputation phase in which the effective parameters are evaluated for all possible considered unit cells, but these can be more difficult to derive for arbitrarily complex microscopic geometries.

We call it "a poor man's approach" because our methodology is based on the exclusive use of the Darcy model, in reference to the paper [67]. As it may be expected, this simplified models lead to significant discrepancies when evaluating the flow field with the full-scale model, typically larger than those observed when using a Brinkman model rather than the Darcy model for solving the state equation (as in [26, 68]). Still, we demonstrate that despite the strongly simplifying assumptions considered, our methodology is able to generate multiscale microchannels designs that achieve reasonable performance, even when evaluated with the full-scale model.

The paper is organized as follows. Section 2 starts by presenting the design problem considered and the associated physical model: we aim at generating a distribution of fluid microchannels spreading over many regularly spaced outlets with uniform output velocity, taking into account upper-bound constraints on the pressure drop and the total fluid volume. We describe the set of admissible locally periodic domains parameterized by two geometric parameters fields and a diffeomorphism.

Before proceeding to a numerical methodology, we present then in Section 3 homogenization results for the Stokes system in an idealized periodic porous medium distorted by a diffeomorphism. We particularly emphasize

the non-trivial dependency of the Darcy matrix to the local grid stretching. The full derivation is based on the method of two-scale expansions and is provided in the Appendix B.1.

Then, in Section 4, we introduce a number of simplifying assumptions that enable us to devise our multiscale design optimization procedure. We provide formulas for the sensitivities of objective and constraint functionals, and we describe filters used to avoid "checkerboard" solutions. Numerical results of the optimization of the geometric parameter fields are presented.

Proceeding in the vein of dehomogenization, which closely follows [40], Section 5 outlines the dehomogenization procedure. We showcase numerically reconstructed designs and evaluate their performance through utilization of the full-scale model. An additional numerical test case with the position of the inlet set at a different location of the domain is presented at the end of the section. In both cases, we obtain satisfactory performance of the reconstructed designs when assessing them to the full-scale model, despite sensible deviations from the predictions of the homogenized model.

Finally, the limitations as well as the perspectives opened by the present work are discussed in the concluding Section 6.

## 2. Setting of the design problem

In this section, we introduce the design problem considered as the physical motivation for the present study. We wish to design a microfluidic device that redistributes an input flow across numerous regularly spaced outlets an output interface, taking advantage of a homogenized description to capture these numerous channels without the need for explicitly representing them on a fine grid.

The design problem is described and modelled as a constrained optimization problem in Section 2.1. The set of admissible designs is restricted to a class of locally periodic media which are constructed according to a procedure detailed in Section 2.2.

### 2.1. Description of the physical model and optimal design problem

In all what follows, we consider a 2D rectangular domain $D = (0,1) \times (0,1)$ illustrated on Figure 1. The domain $D$ is divided into a fluid component $\Omega_\epsilon$ and a solid part $D \backslash \Omega_\epsilon$. The fluid component is labeled by the variable $\epsilon$ which represents a small length scale parameter. The scope of acceptable designs is confined to a class of locally periodic media, which are constructed according to a detailed procedure elaborated in Section 2.2.

A laminar fluid is entering the domain through an inlet boundary $\Gamma_{\text{in}}$ with prescribed velocity $\boldsymbol{u}_\epsilon = \boldsymbol{u}_0$ and flows out the domain through the right boundary $\Gamma_{\text{out}}$ with zero output pressure $p_\epsilon = 0$. In the present setting illustrated on Figure 1, the inlet boundary occupies on a centered portion of the left side of the domain; an alternative configuration with a different inlet position is considered in Section 5.4. The fluid enters the domain

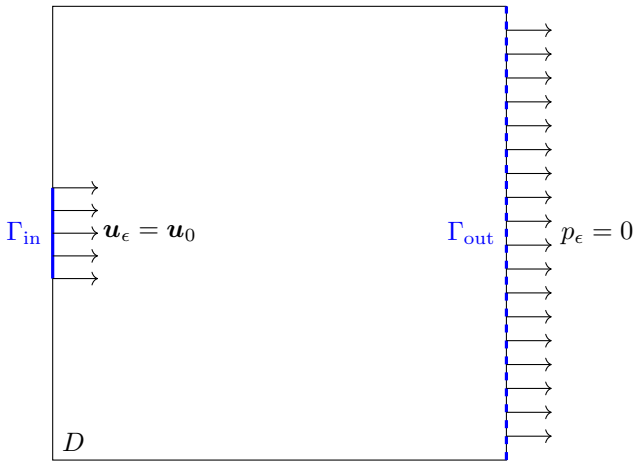


Figure 1. Physical domain $D$ with inlet and outlet boundaries $\Gamma_{\text{in}}$ and $\Gamma_{\text{out}}$.

on the inlet boundary $\Gamma_{\text{in}}$ with velocity $\boldsymbol{u}_\epsilon = \boldsymbol{u}_0$ and exits on the outlet boundary $\Gamma_{\text{out}}$ with zero output pressure $p_\epsilon = 0$ and zero tangential velocity ($\boldsymbol{u}_\epsilon \times \boldsymbol{n} = 0$). We assume that the fluid motion and pressure are governed

by the Stokes equations on $\Omega_\epsilon$, which read:

$$\begin{cases} -\Delta \boldsymbol{u}_\epsilon + \nabla p_\epsilon = 0 \text{ in } \Omega_\epsilon, \\ \operatorname{div}(\boldsymbol{u}_\epsilon) = 0 \text{ in } \Omega_\epsilon, \\ \boldsymbol{u}_\epsilon = \boldsymbol{u}_0 \text{ on } \Gamma_{\text{in}}, \\ \boldsymbol{u}_\epsilon \times \boldsymbol{n} = 0 \text{ on } \Gamma_{\text{out}}, \\ p_\epsilon = 0 \text{ on } \Gamma_{\text{out}}, \\ \boldsymbol{u}_\epsilon = 0 \text{ on } \partial\Omega_\epsilon \backslash (\Gamma_{\text{in}} \cup \Gamma_{\text{out}}). \end{cases} \tag{2.1}$$

We refer to (2.1) as the "full-scale" model. The outlet boundary condition involving the pressure and tangential velocity is rather non-standard but is well-posed, see [23].

The goal is to generate a distribution of microchannels that distribute a fluid in evenly in multiple channels on the right outlet boundary $\Gamma_{\text{out}}$, occupying a limited portion of the domain $D$ and with limited pressure drop. We model the optimal design problem by the following maximization problem

$$\max_{\Omega_\epsilon \subset D} \min_{x \in \Gamma_{\text{out}}} \quad \boldsymbol{u}_\epsilon(x) \cdot \boldsymbol{n}$$
$$s.t. \begin{cases} \texttt{DP}(p) := \displaystyle\int_{\Gamma_{\text{in}}} p_\epsilon \, \mathrm{d}\sigma \le 10 \times \texttt{DP}_0 \times \epsilon^{-2}, \\ \texttt{Vol}(\Omega_\epsilon) := |\Omega_\epsilon| \le \texttt{Vol}_0. \end{cases} \tag{2.2}$$

We use this max-min formulation in the hope that the minimizer yields an approximately constant value for $\boldsymbol{u}(x) \cdot \boldsymbol{n}$ on the outlet boundary $\Gamma_{\text{out}}$. The constants $\texttt{DP}_0$ and $\texttt{Vol}_0$ are given upper bound values for the pressure drop and the volume of the fluid phase $\Omega_\epsilon$ in the bulk domain $D$. The constant $\texttt{DP}_0$ is thought as the pressure drop value in the case where $\Omega_\epsilon = D$, that is without any solid obstacle; in other words, we allow the pressure drop to increase by a maximum factor 10 when adding solid material to the domain. The multiplicative factor $\epsilon^{-2}$ is considered in the pressure drop constraint in order to make the problem (4.5) (approximately) independent of $\epsilon$; the choice of this scaling is motivated by the Darcy model proposed in Section 4 below. Physically, this corresponds to the fact that adding more and more channels makes the pressure drop constraint more difficult to satisfy.

### 2.2. **Description of the locally periodic domain**

To execute topology optimization of the fluid component through the dehomogenization method, we acquire the fluid domain $\Omega_\epsilon \subset D$ by tiling a distorted grid with a locally periodic cell characterized by geometric parameters that change smoothly. In the following, we elaborate on the process for creating such a domain, which draws inspiration from prior dehomogenization studies [9, 41, 62].

We consider the parameterized periodic unit cell $Y(m_1, m_2) = P \backslash T(m_1, m_2)$ illustrated on Figure 2. The cell $Y(m_1, m_2)$ is obtained by removing from the centered unit square $P = (-1/2, 1/2) \times (-1/2, 1/2)$ a rectangle of solid $T(m_1, m_2)$ with dimension $m_1 \times m_2$. The rectangle is centered at the middle of the unit cell. Fluid channels are devised by connecting these cells side-by-side, creating channels of widths $1 - m_1$ and $1 - m_2$ in respectively the vertical and horizontal directions. The choice of this rectangular cell is motivated by its simplicity, it would be of course possible to consider alternative parameterized geometries with rather straightforward adaptations of the method.

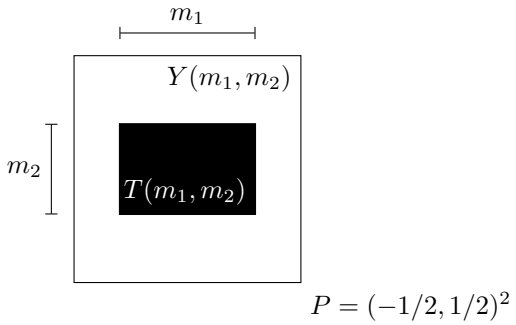


FIGURE 2. A parameterized unit cell for fluid channels. The fluid domain $Y$ is represented in white.

The cells are distributed periodically on a regular grid that is deformed by a nonlinear transformation. Let $\Phi : \mathbb{R}^2 \to \mathbb{R}^2$ be a prescribed diffeomorphism satisfying

$$|\det(\nabla \Phi(X))| \ge c \text{ for all } X \in \mathbb{R}^2,$$

for some positive constant $c > 0$. The map $\Phi$ is understood as a distortion of the cartesian coordinates $X = (X_1, X_2) \in \mathbb{R}^2$. We think of $X = (X_1, X_2)$ as the regular coordinates on the cartesian grid of $\mathbb{R}^2$, and of $x = (x_1, x_2) = \Phi(X)$ as the coordinates on the curved grid. From $\Phi$, we build a multiscale fluid domain by tiling deformed grid cells of size $\epsilon$ with the periodic pattern $Y(m_1, m_2)$, where the geometric parameters $\boldsymbol{m}$ are also allowed to spatially vary smoothly over the domain $D$.

For given smooth distributions of parameters $m_1(\boldsymbol{x})$ and $m_2(\boldsymbol{x})$ and diffeomorphism $\Phi$, we build a locally periodic fluid domain $\Omega_\epsilon$ as the negative subdomain of a level-set function carefully designed. We start by considering a level-set function whose negative domain is $\mathbb{R}^2 \backslash T(m_1, m_2)$ for given fixed parameters $(m_1, m_2)$:

$$\phi(X_1, X_2) = -\max\left(|X_1| - \frac{m_1}{2}, |X_2| - \frac{m_2}{2}\right).$$

We then introduce the sawtooth function $S$ defined by

$$S(t) = t \text{ for } t \in \left]-\frac{1}{2}, \frac{1}{2}\right[ \text{ and } S \text{ is 1–periodic.}$$

The sawtooth function $S$ is plotted on Figure 3; it enables to extend by periodicity a level-set function defining an implicit domain in $(-1/2, 1/2)^2$, a feature which has been used for dehomogenization in [62, 43]. In particular,

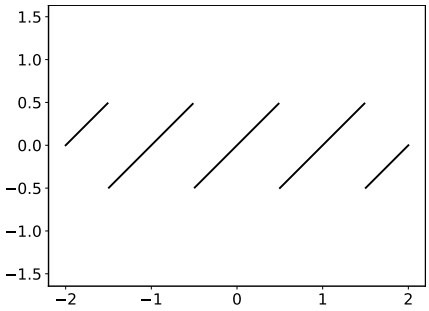


FIGURE 3. Sawtooth function $S$ on $(-2, 2)$.

a level-set function whose negative subdomain is the domain obtained by repeating the cell periodically in the two space directions, that is $P \backslash T(m_1, m_2) + \mathbb{Z}$, is given by

$$(X_1, X_2) \mapsto \phi(S(X_1), S(X_2)).$$

Subsequently, a level-set function whose negative subdomain is the periodic porous structure with periodicity $\epsilon$ aligned on the grid deformed by $\Phi$ (that is $\Phi(\epsilon(Y(m_1, m_2) + \mathbb{Z}))$ is

$$(x_1, x_2) \mapsto \phi\left(S\left(\frac{\Phi_1^{-1}(x_1, x_2)}{\epsilon}\right), S\left(\frac{\Phi_2^{-1}(x_1, x_2)}{\epsilon}\right)\right),$$

where $\Phi_1^{-1}(x_1, x_2)$ and $\Phi_2^{-1}(x_1, x_2))$ denotes the two space components of $\Phi^{-1}(x_1, x_2)$. Finally, a level-set function describing the fluid domain on the curved grid with periodicity $\epsilon$, and spatially modulated parameters $m_1 \equiv m_1(x_1, x_2)$ and $m_2 \equiv m_2(x_1, x_2)$ reads

$$\rho_\epsilon(x_1, x_2) = -\max\left(\left|S\left(\frac{\Phi_1^{-1}(x_1, x_2)}{\epsilon}\right)\right| - \frac{m_1(x_1, x_2)}{2}, \left|S\left(\frac{\Phi_2^{-1}(x_1, x_2)}{\epsilon}\right)\right| - \frac{m_2(x_1, x_2)}{2}\right). \tag{2.3}$$

The negative subdomain of $\rho_\epsilon$ is approximately

$$\{\boldsymbol{x} \in \mathbb{R}^2 \,|\, \rho_\epsilon(\boldsymbol{x}) < 0\} \simeq \bigcup_{\boldsymbol{n} \in \mathbb{Z}} \Phi\Big(\boldsymbol{n}\epsilon + \epsilon T(m_1(\Phi(\boldsymbol{n}\epsilon)), m_1(\Phi(\boldsymbol{n}\epsilon)))\Big),$$

this fact is justified in Appendix A where the interested reader will find an exact explicit description of this set.

Accordingly, the fluid domain $\Omega_\epsilon$ that we consider in (2.1) is defined as the negative subdomain of $\rho_\epsilon$ on $D$:

$$\Omega_\epsilon = \{(x_1, x_2) \in D \,|\, \rho_\epsilon(x_1, x_2) < 0\}. \tag{2.4}$$

The tiling process leading to a domain $\Omega_\epsilon$ is illustrated on Figure 4 for the mapping $\Phi$ whose inverse is given by

$$\Phi^{-1}(x_1, x_2) = \left(\frac{x_1 + 0.3}{(x_1 + 0.3)^2 + (x_2 - 0.5)^2}, -\frac{x_2 - 0.5}{(x_1 + 0.3)^2 + (x_2 - 0.5)^2}\right),$$

and for the distributions of parameters

$$m_1(x_1, x_2) = \max(0, \min(1, x_1^2 + (x_2 - 0.5)^2)), \qquad m_2(x_1, x_2) = \max(0, \min(1, 0.9 - x_1^2)).$$

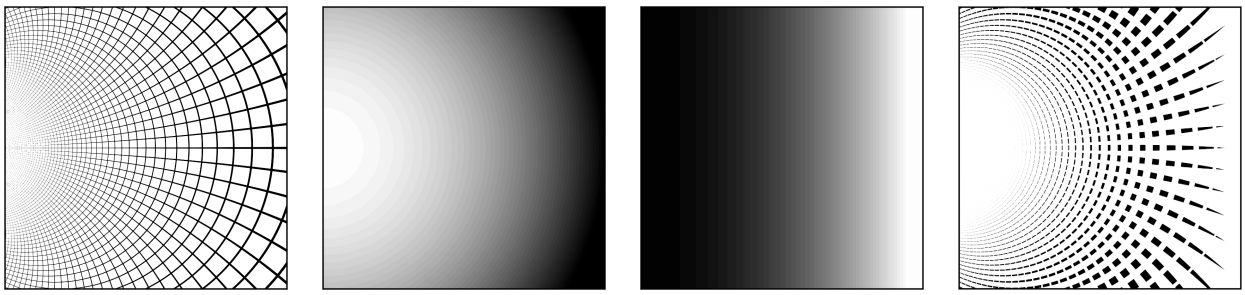

(A) Mapping $\Phi$ (B) $m_1(x_1, x_2)$ (C) $m_2(x_1, x_2)$ (D) $\Omega_\epsilon$.

FIGURE 4. Construction of a locally periodic fluid domain $\Omega_\epsilon$ from a diffeomorphism $\Phi$ and geometric parameter fields $m_1(x_1, x_2)$ and $m_2(x_1, x_2)$ based on the formula (2.3). The colormap for $m_1(x_1, x_2)$ and $m_2(x_1, x_2)$ encompasses values ranging from from 0 to 1 with a gradient transitioning from white to black, so that the fluid domain is represented in white.

## 3. Homogenized permeability matrix on a deformed periodic domain

Rigorous asymptotic expansions of the solution $(\boldsymbol{u}_\epsilon, p_\epsilon)$ to the Stokes problem (2.1) in the perforated domain $\Omega_\epsilon$ are not available in the literature [58, 4, 31], where strictly periodic structures on square domains with homogeneous or Dirichlet boundary conditions are usually considered.

In this section, we state a homogenization result for Stokes flow in deformed periodic domains. We obtain two conclusions: *first*, the flow can be approximated by the solution to a Darcy system with spatially dependent permeability matrix (Proposition 3.1). This could be expected since this result is just a generalization of the standard homogenization theory for periodic porous media where this permeability matrix is constant. For arbitrary deformations, we find that the homogenized Darcy matrix at the point $x \in \Omega_\epsilon$ can be obtained by solving a periodic cell problem in the unit cell stretched by the local Jacobian matrix $\nabla\Phi(\Phi^{-1}(x))$.

*Second*, we find that for conformal deformations, the homogenized Darcy permeability tensor is proportional to the square of the local grid dilation (Proposition 3.2), which is a major difference with respect to the linear elasticity setting where this dilation factor is absent.

We note that there is a rather vast literature on the derivation of homogenized models for non-periodic media: we can mention for instance periodic media with localized defects [15], periodic media with smoothly varying microstructure [22, 6], stochastic media [39], media filled with randomly distributed inclusions [35]. Perforated domains with a locally periodic microstructure defined implicitly as in Section 2.2 have been considered in [21]. On the other hand, locally periodic media obtained by smooth deformation of a periodic medium have been studied in a series of papers [18, 2, 56] that followed a work of Briane [17]. The locally periodic media considered in the work of Briane are very close in spirit to ours, the main difference lies in the fact that we consider the Stokes equation rather than the linear elasticity equation, and that our analysis relies on the introduction of a suitable, non-standard two-scale ansatz (detailed in Appendix B) rather than on various notions of weak convergence. We note that our two-scale expansions method is similar to that of [69] who recently proposed a derivation of the homogenized elasticity system in a deformed periodic medium.

For simplicity, our derivation assumes a simpler setting than the one of Section 2, of that lends itself to rigorous asymptotic expansions. Let $K = (0, 1)^2$ be the unit square domain understood as a portion of $\mathbb{R}^2$. We use a different notation than $D$ (or $P$) to avoid any confusion with respect to Section 2: here, $K$ is the argument space of the diffeomorphism $\Phi$ while the computational domain $D$ is the argument space of $\Phi^{-1}$ in Section 2. We denote by $K_\epsilon = K \backslash \omega_\epsilon$ the set obtained by perforating $K$ with holes $\omega_\epsilon = \epsilon(P \backslash T(m_1, m_2) + \mathbb{Z}^2)$ periodically distributed on a regular grid of width $\epsilon$. We then consider a laminar fluid flowing in the distorted domain $\Phi(K_\epsilon)$ illustrated on Figure 5.

In this section only, we assume that the parameters $m_1$ and $m_2$ are constant: the shape of the hole $T(m_1, m_2)$ is not modulated along the domain; we only investigate the effect of the distortion of the domain by the diffeomorphism $\Phi$. Actually, the solid obstacles may have an arbitrarily different shape than the one of Figure 2, but this shape is not spatially modulated along the domain.

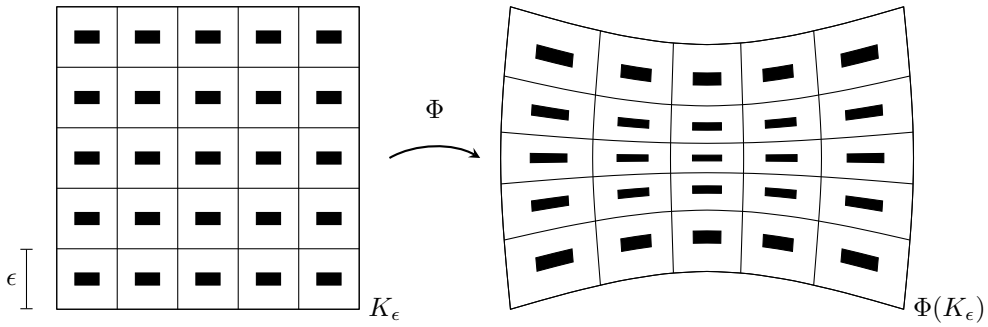


FIGURE 5. Deformed periodic domain $\Phi(K_\epsilon)$.

For the present analysis, we assume that the flow is governed by the Stokes system in the deformed perforated domain $\Omega_\epsilon = \Phi(K_\epsilon)$ with periodic boundary conditions on opposite deformed matching faces:

$$\begin{cases} -\Delta \boldsymbol{u}_\epsilon + \nabla p_\epsilon = \boldsymbol{f} \text{ in } \Phi(K_\epsilon), \\ \qquad \operatorname{div}(\boldsymbol{u}_\epsilon) = 0 \text{ in } \Phi(K_\epsilon), \\ \qquad\qquad \boldsymbol{u}_\epsilon = 0 \text{ on } \Phi(\partial\omega_\epsilon), \\ \displaystyle\int_{\Phi(K_\epsilon)} p_\epsilon \,\mathrm{d}x = 0, \\ \qquad\qquad \boldsymbol{u}_\epsilon \circ \Phi \text{ is } K\text{–periodic}, \end{cases} \tag{3.1}$$

where $\boldsymbol{f}$ is a given a smooth right-hand side forcing and where we impose that the pressure has zero average to fix the constant.

In order to state our homogenization result for (3.1), let us introduce, for a given $x \in \Phi(K)$, the solution $(\boldsymbol{\mathcal{X}}_j(x,\cdot), \alpha_j(x,\cdot))_{1\le j\le 2}$ to the following cell problem posed in the linearly stretched cell $\nabla\Phi(\Phi^{-1}(x))Y(m_1,m_2)$:

$$\begin{cases} -\Delta_{zz}\boldsymbol{\mathcal{X}}_j(x,z) + \nabla_z \alpha_j(x,z) = \boldsymbol{e}_j \qquad \forall z \in \nabla\Phi(\Phi^{-1}(x))Y(m_1,m_2), \\ \qquad\qquad \operatorname{div}_z(\boldsymbol{\mathcal{X}}_j(x,z)) = 0 \qquad \forall z \in \nabla\Phi(\Phi^{-1}(x))Y(m_1,m_2), \\ \displaystyle\int_{\nabla\Phi(\Phi^{-1}(x))Y(m_1,m_2)} \alpha_j(x,z)\,\mathrm{d}z = 0, \\ \qquad\qquad \boldsymbol{\mathcal{X}}_j(x,z) = 0 \qquad \forall z \in \partial(\nabla\Phi(\Phi^{-1}(x))T), \\ \qquad\qquad \boldsymbol{\mathcal{X}}_j(x,\cdot) \text{ is } \nabla\Phi(\Phi^{-1}(x))P\text{–periodic}, \end{cases} \tag{3.2}$$

where $\boldsymbol{e}_1 = (1,0)$ and $\boldsymbol{e}_2 = (0,1)$ denote the vectors of the canonical basis of $\mathbb{R}^2$. The stretched cell $\nabla\Phi(\Phi^{-1}(x))Y(m_1,m_2)$ is illustrated on Figure 6. It reflects that as $\epsilon \to 0$, infinitesimally small cells of width $\epsilon$ are deformed by the linear Jacobian $\nabla\Phi$. When the transformation $\Phi$ is the identity mapping, the cell problem (3.2) reduces to the standard cell problem derived by homogenization theory in the Darcy regime [58].

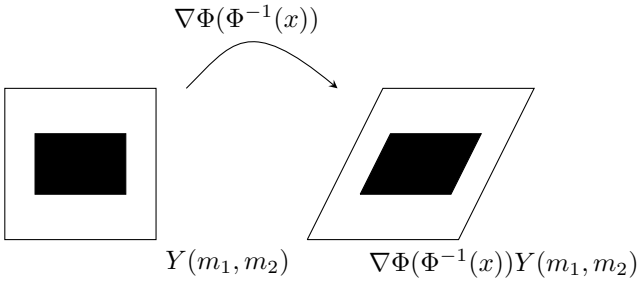


FIGURE 6. Deformation of the unit cell by the linearized transformation.

We then denote by

$$\mathcal{X}(x,\cdot) = \begin{bmatrix} \boldsymbol{\mathcal{X}}_1(x,\cdot) & \boldsymbol{\mathcal{X}}_2(x,\cdot) \end{bmatrix} \tag{3.3}$$

the matrix gathering the cell solutions and we introduce the *permability matrix* $\mathcal{X}^*(x) = (\mathcal{X}^*_{ij}(x))_{1\le i,j\le 2}$ obtained by averaging $\mathcal{X}(x,\cdot)$ over the unit cell:

$$\mathcal{X}^*_{ij}(x) = \frac{1}{|\nabla\Phi(\Phi^{-1}(x))P|} \int_{\nabla\Phi(\Phi^{-1}(x))Y(m_1,m_2)} \boldsymbol{e}_i^T \boldsymbol{\mathcal{X}}_j(x,z)\,\mathrm{d}z, \qquad \forall 1 \le i,j \le 2. \tag{3.4}$$

The coefficients of the permeability matrix $\mathcal{X}^*$ are normalized by the area of the deformed unit cell $|\nabla\Phi(\Phi^{-1}(x))P|$.

The following proposition states that the system (3.1) can be homogenized and that the homogenized velocity and pressure are at first order solution to a Darcy system with inhomogeneous porosity tensor $\mathcal{X}^*_{ij}(x)$.

**Proposition 3.1.** *Let $(\boldsymbol{u}, p)$ be the solution to the following Darcy system:*

$$\begin{cases} \boldsymbol{u}(x) = \mathcal{X}^*(x)(\boldsymbol{f}(x) - \nabla p(x)), & x \in \Phi(K), \\ \operatorname{div}(\boldsymbol{u}(x)) = 0, & x \in \Phi(K), \\ \displaystyle\int_{\Phi(K)} p(x)\,\mathrm{d}x = 0, \\ \boldsymbol{u},\ p \text{ are } \Phi(K) \text{ periodic}, \end{cases} \tag{3.5}$$

*where $\mathcal{X}^*$ is the permeability matrix (3.4). Then the following asymptotic expansions hold for the solution $(\boldsymbol{u}_\epsilon, p_\epsilon)$ to the perforated Stokes system (3.1) in the deformed domain $\Phi(K_\epsilon)$:*

$$\boldsymbol{u}_\epsilon(x) = \epsilon^2 \mathcal{X}(x, \nabla\Phi(\Phi^{-1}(x))\Phi^{-1}(x)/\epsilon)(\boldsymbol{f}(x) - \nabla p(x)) + O(\epsilon^3), \qquad p_\epsilon(x) = p(x) + O(\epsilon), \tag{3.6}$$

*where $\mathcal{X}(x, \cdot)$ is the matrix (3.3) and the error terms are measured with the $L^2$ norm on $\Phi(K_\epsilon)$.*

*Proof.* The proof is based on the method of two-scale expansions and is detailed in Appendix B.1. □

Equation (3.6) shows that the functions $\epsilon^2\boldsymbol{u}(x)$ and $p(x)$ of (3.5) are the leading order approximations of $\boldsymbol{u}_\epsilon$ with the oscillations at the small scale $\epsilon$ being averaged. The model (3.5) is therefore a homogenized model for (3.1) with effective permeability matrix $\mathcal{X}^*(x)$.

We now stress an important difference with respect to the mechanical setting. In the works [9, 41] dealing with dehomogenization of mechanical structure, the deformation $\Phi$ is assumed to be a conformal mapping, namely preserving locally right angles at the grid intersections. The conformality condition means that the polar decomposition of the Jacobian matrix $\Phi(x)$ has the form

$$\nabla\Phi(\Phi^{-1}(x)) = s(x)R(x), \tag{3.7}$$

for real positive number $s(x) > 0$ and orthogonal $2 \times 2$ matrix $R(x)$ satisfying $R(x)^T R(x) = I$. In the present situation, we find that the Darcy matrix $\mathcal{X}^*(x)$ admits a simple expression when $\Phi$ is a conformal mapping.

**Proposition 3.2.** *Assume that $\Phi$ is a conformal mapping satisfying (3.7). Then the permeability matrix $\mathcal{X}^*(x)$ of (3.4) admits the following expression:*

$$\mathcal{X}^*(x) = s(x)^2 R(x)\mathcal{X}^* R(x)^T. \tag{3.8}$$

*where $\mathcal{X}^* = (\mathcal{X}^*_{ij})_{1\le i,j\le 2}$ is the Darcy tensor of the non-deformed unit cell $Y(m_1, m_2)$, namely*

$$\mathcal{X}^*_{ij} = \int_{Y(m_1,m_2)} \boldsymbol{e}_i^T \boldsymbol{\mathcal{X}}_j(y)\,\mathrm{d}y, \qquad 1 \le i, j \le 2, \tag{3.9}$$

*where $(\boldsymbol{\mathcal{X}}_j)_{1\le i,j\le 2}$ are the solutions to the cell problem in the unit square cell $Y(m_1, m_2) = P\backslash T(m_1, m_2)$:*

$$\begin{cases} -\Delta_{yy}\boldsymbol{\mathcal{X}}_j + \nabla\alpha_j = \boldsymbol{e}_j \text{ in } Y(m_1, m_2), \\ \operatorname{div}(\boldsymbol{\mathcal{X}}_j) = 0 \text{ in } Y(m_1, m_2), \\ \displaystyle\int_{Y(m_1,m_2)} \alpha_j(y)\,\mathrm{d}y = 0, \\ \boldsymbol{\mathcal{X}}_j = 0 \text{ on } \partial T, \\ \boldsymbol{\mathcal{X}}_j \text{ is } P\text{–periodic}. \end{cases} \tag{3.10}$$

*Proof.* The proof is given in Appendix B.2. □

The scaling $s^2(x)$ affecting the homogenized permeability tensor $\mathcal{X}^*(x)$ is a major difference with respect to the linear elasticity setting. In the case of homogenized elasticity tensor within a deformed periodic domain, a relationship similar to (3.8) holds, albeit devoid the dilation factor $s(x)$ [9]. This observation signifies that conventional dehomogenization techniques [9, 41], which assume the homogenized tensor's dependence solely on local orientation (i.e., the matrix $R(x)$) and not on local grid stretching $s(x)$, need to be revisited theoretically for dehomogenizing porous media. However, we do not address this challenge within the scope of this paper.

Alternatively, in the subsequent analysis, we opt to disregard the influence of the local grid stretching $s(x)$. This simplification permits the application of existing dehomogenization methods to tackle the design problem described in Section 2.

## 4. Optimal design of fluid microchannels with an approximate homogenized Darcy model

In this section, we present a numerical approach to tackle the design optimization problem (2.2) that takes advantage of a multiscale model. Building upon the insights from the previous section's analysis, we propose a heuristic homogenized model in Section 4.1 that incorporates several simplifying assumptions to facilitate the application of the dehomogenization method as described in [9, 41].

Following this, Section 4.2 describes the offline precomputation phase, in which we compute the coefficients of the permeability matrix by solving cell problems corresponding to various cell geometries. The subsequent Section 4.3 outlines the derivation of formulas necessary for calculating the derivatives of both the objective and constraint functions which are required by first-order optimization techniques.

Finally, we realize in Section 4.4 that checkerboard patterns emerge when solving the constrained optimization problem. This leads us to resort to density filters in order to acquire smooth geometric parameter distributions and orientation fields. We also use an additional filter to project the design to well delimited pure solid, pure fluid, or porous regions. Solving numerically the optimization problem, we obtain optimized distributions of geometric channel spacings $m_1$, $m_2$ and orientation field $\theta$ that are dehomogenized in the next Section 5.

### 4.1. Simplified relaxation of the design problem

We make the hypothesis that the fluid velocity and pressure $(\boldsymbol{u}_\epsilon, p_\epsilon)$ solution to the full-scale model (2.1) can be approximated (in an approximate homogenized sense that we leave unclarified) by the solution $(\boldsymbol{u}, p)$ to the following Darcy system:

$$\begin{cases} \boldsymbol{u} = -\epsilon^2 \mathcal{X}^*(m_1, m_2, \theta)\nabla p, & \text{in } D, \\ \operatorname{div}(\boldsymbol{u}) = 0 & \text{in } D, \\ \boldsymbol{u}\cdot\boldsymbol{n} = \boldsymbol{u}_0\cdot\boldsymbol{n} & \text{on } \Gamma_{\text{in}}, \\ p = 0 & \text{on } \Gamma_{\text{out}}, \end{cases} \tag{4.1}$$

where $\mathcal{X}^*(m_1, m_2, \theta)$ denotes the permeability matrix given by

$$\mathcal{X}^*(m_1, m_2, \theta) := R(\theta)\mathcal{X}^*(m_1, m_2)R(\theta)^T, \tag{4.2}$$

with $\mathcal{X}^*(m_1, m_2)$ being the permeability tensor as defined in (3.9) within the parameterized cell $Y(m_1, m_2)$ depicted in Figure 2. The matrix $R(\theta)$ is the one arising in the polar decomposition of $\nabla\Phi(\Phi^{-1}(x))$ as in (3.7) and is represented as

$$R(\theta) = \begin{bmatrix} \cos(\theta) & -\sin(\theta) \\ \sin(\theta) & \cos(\theta) \end{bmatrix},$$

where $\theta$ is the orientation parameter. It's important to note that in Equation (4.2), $m_1$, $m_2$, and $\theta$ are parameters that vary with spatial position.

In our implementation, we solve the Darcy system (4.1) by solving the equivalent Laplace equation for the pressure $p$ with a Neumann boundary condition on $\Gamma_{\text{in}}$ and a Dirichlet boundary condition on $\Gamma_{\text{out}}$:

$$\begin{cases} -\operatorname{div}(\mathcal{X}^*(m_1, m_2, \theta)\nabla p) = 0 & \text{in } D, \\ \boldsymbol{n}^T\mathcal{X}^*(m_1, m_2, \theta)\nabla p = -\epsilon^{-2}\boldsymbol{u}_0\cdot\boldsymbol{n} & \text{on } \Gamma_{\text{in}}, \\ p = 0 & \text{on } \Gamma_{\text{out}}. \end{cases} \tag{4.3}$$

Note that $p$ is proportional to $\epsilon^{-2}$ and the velocity field $\boldsymbol{u}$ determined by (4.1) is independent of the parameter $\epsilon$.

We numerically solve (4.3) with the finite element method, by discretizing the following variational formulation: find $p \in H^1(D)$ with $p = 0$ on $\Gamma_{\text{out}}$ such that for any $q \in H^1(D)$ with $q = 0$ on $\Gamma_{\text{out}}$:

$$\int_D \mathcal{X}^*(m_1, m_2, \theta)\nabla p\cdot\nabla q \,\mathrm{d}x = -\epsilon^{-2}\int_{\Gamma_{\text{in}}} (\boldsymbol{u}_0\cdot\boldsymbol{n})q \,\mathrm{d}\sigma, \tag{4.4}$$

where $H^1(D)$ is the standard Sobolev space of square integrable functions with square integrable partial derivatives on $D$.

We then approximate the design problem (2.2) by the following "relaxed" version

$$\max_{\substack{0\le m_1, m_2\le 1 \\ \theta\in\mathbb{R}}} \quad \texttt{MINOUT}(\boldsymbol{u}) := \left(\frac{1}{|\Gamma_{\text{out}}|}\int_{\Gamma_{\text{out}}} (\boldsymbol{u}\cdot\boldsymbol{n})^{-\mathtt{p}}\,\mathrm{d}\sigma\right)^{-\frac{1}{\mathtt{p}}}$$
$$s.t. \begin{cases} \texttt{DP}(p) = \displaystyle\int_{\Gamma_{\text{in}}} p\,\mathrm{d}\sigma \le 10\times\texttt{DP}_0\times\epsilon^{-2}, \\ \texttt{Vol}(m_1, m_2) = \displaystyle\int_D (1 - m_1 m_2)\,\mathrm{d}x \le \texttt{Vol}_0, \end{cases} \tag{4.5}$$

where the pressure drop constant is set to $\texttt{DP}_0 = 1$ and $\mathtt{p}$ is a penalty parameter set to $\mathtt{p} = 4$ in our implementation.

The multiplicative factor $\epsilon^{-2}$ considered in the pressure drop constraint makes the optimization problem (4.5) independent of $\epsilon$. Thus, in our numerical implementation, we solve the state and the optimization problem (4.3) and (4.5) with $\epsilon = 1$.

It is important to note that the homogenized model (4.1) and the relaxed optimization problem (4.5) introduce multiple approximations. First, the effective model (4.1) is heuristic, in the sense that:

- it assumes the transformation $\Phi$ to be conformal (preserving right angles) and the dilation parameter to be constant ($s(x) = 1$ in (3.8)) for (4.2) to hold true. in order for (4.2) to be true. In other words, it assumes that
$$\nabla\Phi(\Phi^{-1}(x)) \simeq R(\theta(x)) \text{ for all } x \in D. \tag{4.6}$$
However such approximation cannot be valid without a definite amount of error, since (4.6) is possible only for approximately rigid body transformations (see [47]);
- it is not valid in the low volume fraction limit $m_1$ and $m_2 \to 0$ corresponding to locations where the solid obstacles disappear (see [3, 34]) where the Darcy model (4.3) becomes singular (the coefficients of $\mathcal{X}^*(m_1, m_2)$ blow up as $m_1$ and $m_2 \to 0$, and converges to zero as $m_1$ and $m_2 \to 1$). We decide to neglect the transition to the Stokes regime occurring in this regime. We numerically assign the coefficients of $\mathcal{X}^*$ to finite values when $m_1, m_2$ approach 0 and 1, these values being chosen by interpolation (see Section 4.2);
- it potentially neglects boundary layers arising in the vicinity of $\partial D$ due to the inlet, wall and outlet boundary conditions in (2.1).

Second, the minimum of $\boldsymbol{u}_\epsilon \cdot \boldsymbol{n}$ on $\Gamma_{\text{out}}$ in (2.2) is approximated by the differentiable averaged functional `MINOUT` with penalty parameter $\mathtt{p} = 4$.

*Remark* 4.1. The volume functional $\mathtt{Vol}(m_1, m_2)$ is a consistent approximation of the fluid volume $|\Omega_\epsilon|$, see the discussion at the end of Appendix A. This approximation has also been used in [9, 41] and has shown to be accurate when dehomogenizing mechanical structures.

### 4.2. **Offline phase: precomputation of the Darcy permeability matrix**

In order to solve the Poisson problem (4.3) and to evaluate the objective function `MINOUT` and its derivatives, we precompute the Darcy matrix $\mathcal{X}^*(m_1, m_2)$ as well as its partial derivatives in a preliminary offline phase. This step is computationally expensive as it involves solving many times the cell-problem (3.10) but is required only once before solving any optimization problem depending on the variables $\boldsymbol{u}$ and $p$. Furthermore, the computational time can be diminished by solving the cell problems independently in parallel.

The coefficients of the permeability matrix are evaluated for all possible combinations of parameters $(m_1, m_2)$ distributed on a grid discretizing $(0, 1) \times (0, 1)$ with 100 points, removing 0 and 1 corresponding to degeneracies (respectively a crack in the cell and a cell full of solid). The partial derivatives of $\mathcal{X}^*(m_1, m_2)$ with respect to $m_1$ and $m_2$ are estimated using finite differences. Then, a linear interpolant is constructed for approximating this tensor in the whole square $(0, 1) \times (0, 1)$. The orientation-dependent permeability tensor $\mathcal{X}^*(m_1, m_2, \theta)$ is subsequently obtained thanks to the formula (4.2). Since the cell is symmetric with respect to the median axes, $\mathcal{X}^*$ is a diagonal matrix and only the coefficients $\mathcal{X}^*_{11}$ and $\mathcal{X}^*_{22}$ needs to be computed.

For a set of given parameters $(m_1, m_2)$, the matrix $\mathcal{X}^*(m_1, m_2)$ is computed with formula (3.9) after solving the cell problem (3.10). Each cell problem is solved by the finite element method with FreeFEM [46, 1] on a single periodic mesh with the rectangle $T(m_1, m_2)$ explicitly discretized using the remeshing software MMg [24]. The typical edge length defining the mesh resolution is $\mathtt{h} = 0.01$. We solve the matrix-block formulation of the Stokes system using a Lagrange multiplier to enforce the zero-mean constraint for the pressure, and a PETSc fieldsplit Schur preconditioner [11] for solving the linear system.

We illustrate on Figure 7 a coarse version of the mesh employed for discretizing a unit cell $Y(m_1, m_2)$ and the vector fields $\boldsymbol{\mathcal{X}}_1$ and $\boldsymbol{\mathcal{X}}_2$ solutions to the cell problem (3.10) evaluated on this mesh.

Surface plots of the diagonal coefficients $\mathcal{X}^*_{11}$ and $\mathcal{X}^*_{22}$ computed in this offline phase are represented on Figure 8. As expected, coefficients are vanishing near the point $(1, 1)$ (corresponding to pure solid regions) and reach a maximal value the point $(0, 0)$ (corresponding to pure fluid regions).

*Remark* 4.2. In theory, $\mathcal{X}^*_{11}$ and $\mathcal{X}^*_{22}$ blow up as $m_1$ and $m_2 \to 0$, which is not obtained numerically since, as visible on Figure 8, the interpolation procedure sets these coefficients to a value approximately equal to 0.35 near the point (0,0). This is related to the fact that $\mathcal{X}^*_{11}$ and $\mathcal{X}^*_{22}$ scale as $|\log \eta|$ for a rescaled obstacle of size $\eta m_1 \times \eta m_2$ [3]. In order to amplify the permeability tensor by a multiplicative factor $C$, $\eta$ needs to be roughly of the order of $10^{-C}$, which is difficult to achieve numerically. Physically, this is related to the fact that in 2D, exponentially small obstacles have a non-negligible influence on the flow-field (corresponding to the Brinkman regime). This amounts to say that our Darcy model assumes that pure fluid regions are in fact not "pure fluid" but filled with very tiny obstacles. We verified that the numerical procedure devised in the next sections is rather insensitive to setting manually $\mathcal{X}^*_{11}$ and $\mathcal{X}^*_{22}$ to a large constant for $m_1 = m_2 = 0$.

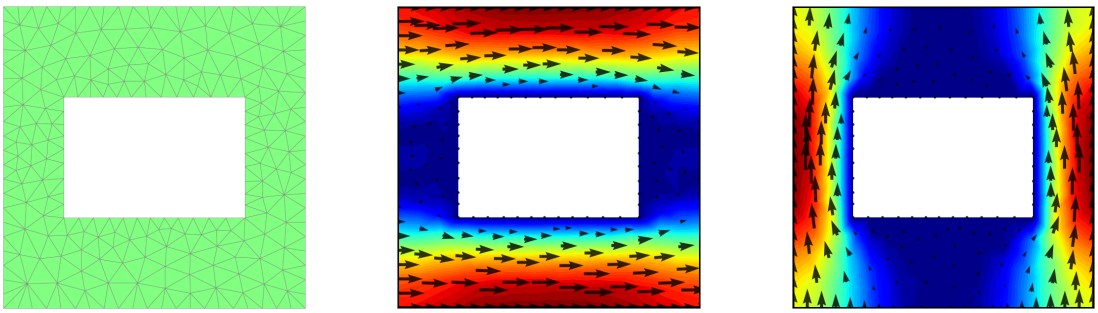

(A) Mesh of a unit cell (B) $\boldsymbol{\mathcal{X}}_1$ (C) $\boldsymbol{\mathcal{X}}_2$

FIGURE 7. Solutions to the cell problem (3.10) on a periodic mesh.

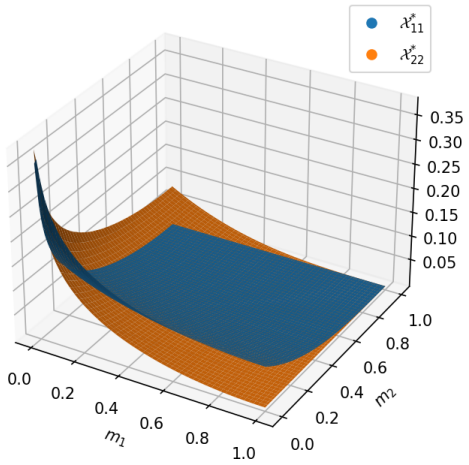


FIGURE 8. 3D plot of the coefficients $\mathcal{X}^*_{11}$ and $\mathcal{X}^*_{22}$ for $(m_1, m_2) \in (0,1) \times (0,1)$.

### 4.3. **Adjoint-based numerical optimization**

We use the open-source implementation [30] of the Null Space Optimizer [33, 32] as a first order gradient method for solving the optimization program (4.5). The algorithm requires the Fréchet derivatives of the objective and constraint functions, which can be computed by using the formula of the next proposition.

**Proposition 4.1.** *Let us denote by* $\boldsymbol{m} := (m_1, m_2, \theta) \in L^\infty(D, (0,1) \times (0,1) \times \mathbb{R})$. *Let* $J(\boldsymbol{m}, p)$ *be a Fréchet differentiable functional with respect to* $\boldsymbol{m}$ *and* $p \in H^1(D)$ *and denote by* $p \equiv p(\boldsymbol{m}) \in H^1(D)$ *the solution to the Poisson equation* (4.3). *The mapping* $\boldsymbol{m} \mapsto J(\boldsymbol{m}, p(\boldsymbol{m}))$ *is Fréchet differentiable and the Fréchet derivative is given by*

$$\frac{\mathrm{d}}{\mathrm{d}\boldsymbol{m}}[J(\boldsymbol{m}, p(\boldsymbol{m}))] \cdot \delta\boldsymbol{m} = \frac{\partial J}{\partial \boldsymbol{m}}(\boldsymbol{m}, p(\boldsymbol{m})) \cdot \delta\boldsymbol{m} - \int_D \frac{\partial \mathcal{X}^*}{\partial \boldsymbol{m}}(\boldsymbol{m}) \cdot \delta\boldsymbol{m} \nabla p \cdot \nabla q \, \mathrm{d}x, \tag{4.7}$$

*where* $q$ *is the solution to the adjoint problem*

*find* $q \in H^1(D)$ *with* $q = 0$ *on* $\Gamma_{\text{out}}$ *such that*

$$\int_D \mathcal{X}^*(\boldsymbol{m}) \nabla q \cdot \nabla q' \, \mathrm{d}x = \frac{\partial J}{\partial p}(\boldsymbol{m}, p(\boldsymbol{m})) \cdot q' \text{ for all } q' \in H^1(D) \text{ with } q' = 0 \text{ on } \Gamma_{\text{out}}. \tag{4.8}$$

*Proof.* We compute the derivative of $J(\boldsymbol{m}, p(\boldsymbol{m}))$ by following the classical steps of the adjoint method. Using the chain rule, we find

$$\frac{\mathrm{d}}{\mathrm{d}\boldsymbol{m}}[J(\boldsymbol{m}, p(\boldsymbol{m}))] \cdot \delta\boldsymbol{m} = \frac{\partial J}{\partial \boldsymbol{m}}(\boldsymbol{m}, p(\boldsymbol{m})) \cdot \delta\boldsymbol{m} + \frac{\partial J}{\partial p}(\boldsymbol{m}, p(\boldsymbol{m})) \cdot \left( \frac{\mathrm{d}p}{\mathrm{d}\boldsymbol{m}}(\boldsymbol{m}) \cdot \delta\boldsymbol{m} \right).$$

Differentiating (4.4) with respect to $\boldsymbol{m} = (m_1, m_2, \theta)$, we find that $\frac{\mathrm{d}p}{\mathrm{d}\boldsymbol{m}}(\boldsymbol{m}) \cdot \delta\boldsymbol{m}$ satisfies

$$\int_D \mathcal{X}^*(\boldsymbol{m}) \nabla \left( \frac{\mathrm{d}p}{\mathrm{d}\boldsymbol{m}}(\boldsymbol{m}) \cdot \delta\boldsymbol{m} \right) \cdot \nabla q \, \mathrm{d}x = - \int_D \frac{\mathrm{d}\mathcal{X}^*}{\mathrm{d}\boldsymbol{m}}(\boldsymbol{m}) \cdot \delta\boldsymbol{m} \nabla p \cdot \nabla q \, \mathrm{d}x.$$

Finally, (4.7) follows by substituting $q' = \frac{\mathrm{d}p}{\mathrm{d}\boldsymbol{m}} \cdot \delta\boldsymbol{m}$ in (4.8) and by using the symmetry of the matrix $\mathcal{X}^*(\boldsymbol{m})$. □

In our particular case, we rewrite $\texttt{MINOUT}(\boldsymbol{u})$ in terms of $p$ as

$$\texttt{MINOUT}(\boldsymbol{u}) \equiv \texttt{MINOUT}(\boldsymbol{m}, p) = \left( \frac{1}{|\Gamma_{\text{out}}|} \int_{\Gamma_{\text{out}}} (\epsilon^2 \boldsymbol{n}^T \mathcal{X}^*(\boldsymbol{m}) \nabla p)^{-\mathtt{p}} \right)^{-\frac{1}{\mathtt{p}}}. \tag{4.9}$$

We do not delve into the mathematical issue of the trace of $\nabla p \in L^2(D)$ being not well defined on $\Gamma_{\text{out}}$ when writing this formula, that turns out to behave rather well numerically. The Fréchet derivatives of the functional $\texttt{MINOUT}(\boldsymbol{m}, p)$ of (4.9), the pressure drop functional $\texttt{DP}(p)$ and the volume functional $\texttt{Vol}(m_1, m_2)$ can then be assembled with (4.7) and (4.8) from their partial derivatives:

$$\begin{aligned} \frac{\partial \texttt{MINOUT}}{\partial \boldsymbol{m}}(\boldsymbol{m}, p) \cdot \delta \boldsymbol{m} = \epsilon^2 \left( \frac{1}{|\Gamma_{\text{out}}|} \int_{\Gamma_{\text{out}}} (\boldsymbol{n}^T \mathcal{X}^*(\boldsymbol{m}) \nabla p)^{-\mathtt{p}} \, \mathrm{d}\sigma \right)^{-\frac{1}{\mathtt{p}}-1} \\ \times \frac{1}{|\Gamma_{\text{out}}|} \int_{\Gamma_{\text{out}}} \left( \boldsymbol{n}^T \left( \frac{\partial \mathcal{X}^*}{\partial \boldsymbol{m}} \cdot \delta \boldsymbol{m} \right) \nabla p \right) (\boldsymbol{n}^T \mathcal{X}^*(\boldsymbol{m}) \nabla p)^{-\mathtt{p}-1} \, \mathrm{d}\sigma, \end{aligned} \tag{4.10}$$

$$\begin{aligned} \frac{\partial \texttt{MINOUT}}{\partial p}(\boldsymbol{m}, p) \cdot \delta p = \epsilon^2 \left( \frac{1}{|\Gamma_{\text{out}}|} \int_{\Gamma_{\text{out}}} (\boldsymbol{n}^T \mathcal{X}^*(\boldsymbol{m}) \nabla p)^{-\mathtt{p}} \, \mathrm{d}\sigma \right)^{-\frac{1}{\mathtt{p}}-1} \\ \times \frac{1}{|\Gamma_{\text{out}}|} \int_{\Gamma_{\text{out}}} \left( \boldsymbol{n}^T \mathcal{X}^*(\boldsymbol{m}) \nabla (\delta p) \right) (\boldsymbol{n}^T \mathcal{X}^*(\boldsymbol{m}) \nabla p)^{-\mathtt{p}-1} \, \mathrm{d}\sigma. \end{aligned} \tag{4.11}$$

$$\frac{\partial \texttt{DP}}{\partial p}(p) \cdot \delta p = \int_{\Gamma_{\text{in}}} \delta p \, \mathrm{d}\sigma,$$

$$\frac{\partial \texttt{Vol}(m_1, m_2)}{\partial m_1} \cdot (\delta m_1) = -\int_D m_2 \times \delta m_1 \, \mathrm{d}x, \qquad \frac{\partial \texttt{Vol}(m_1, m_2)}{\partial m_2} \cdot (\delta m_2) = -\int_D m_1 \times \delta m_2 \, \mathrm{d}x,$$

### 4.4. **Checkerboard effect and filtering of the design variable**

Solving the optimization problem (4.5) as it is formulated yields numerical designs featuring checkerboard patterns. The checkerboard effect is a classical phenomenon in density based Topology Optimization [59]; it reflects the fact that numerical designs discontinuous across mesh elements are more performant than smooth designs. However, this effect is not desirable since this gain of performance is a pure artefact of the numerical discretization, and the dehomogenization method requires geometric parameters and orientation fields to vary smoothly over the meshed domain $D$.

We illustrate this effect in the present case on Figure 10 where we display the parameter fields $m_1$, $m_2$ and $\theta$ optimized on a regular triangle mesh $\mathcal{T}_{\text{coarse}}$ with edge length $h_{\text{coarse}} = 1/60$ (Figure 9). These parameters feature large areas with checkerboard patterns near the outlet boundary $\Gamma_{\text{out}}$. Additionally, the objective function is very sensitive to very small variations of the design preventing a smooth convergence of the optimization process: after increasing as expected till iteration 80, the objective function suddenly shrinks to suboptimal values, as visible on Figure 11.

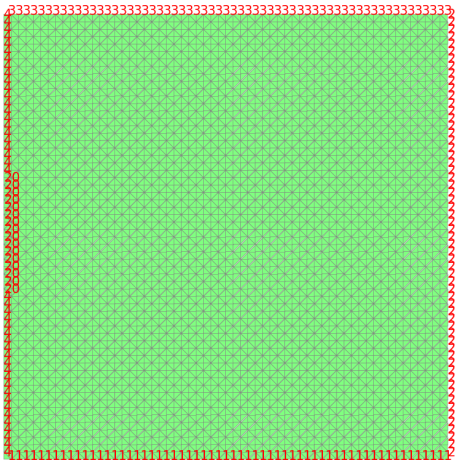

FIGURE 9. Computational mesh for solving the optimization problem (4.5) on the square domain $D = (0, 1)$ with boundaries $\Gamma_{\text{in}}$ and $\Gamma_{\text{out}}$ respectively labeled by 20 and 2.

This issue is almost solved when using a Hilbertian inner product for identifying the gradient, namely when filtering sensitivities by solving the variational problem

$$\text{find } \nabla J(\boldsymbol{m}, p(\boldsymbol{m})) \in H^1(D) \text{ such that } \forall v \in H^1(D), \quad a(\nabla J, v) = \mathrm{D}J(\boldsymbol{m}, p(\boldsymbol{m})) \cdot v, \tag{4.12}$$

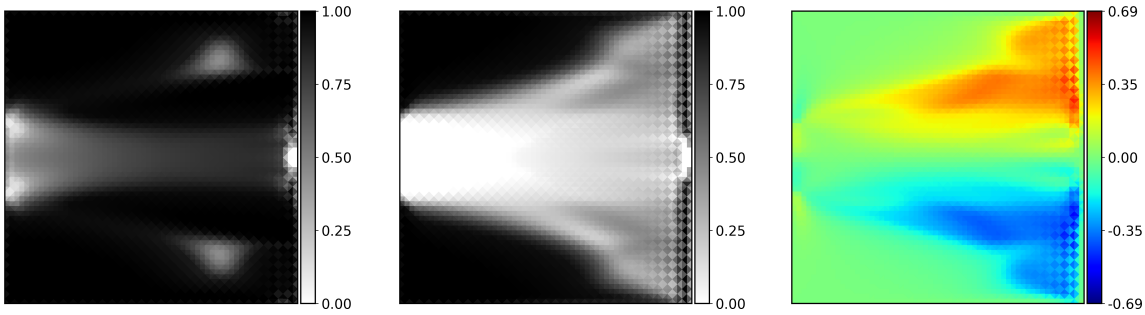


(A) $m_1$ (B) $m_2$ (C) $\theta$

FIGURE 10. Optimized design variables $(m_1, m_2, \theta)$ obtained after 200 iterations of the Null Space Optimizer solving the optimization problem (4.5) without filtering.

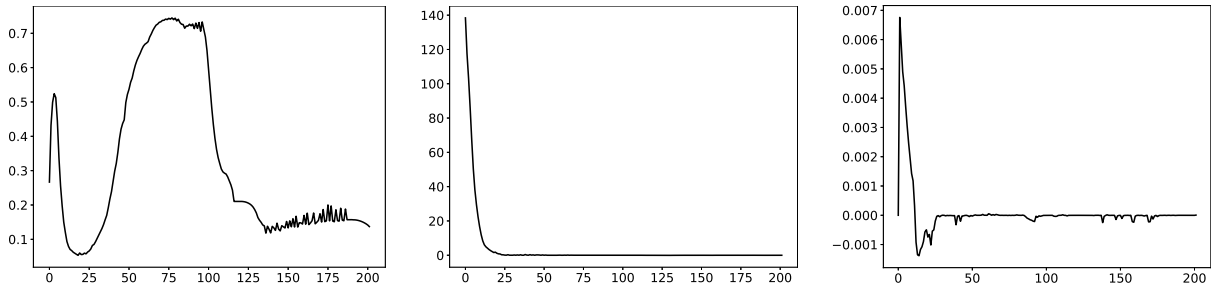


(A) Maximized objective function `MINOUT` (B) $\texttt{DP}/\texttt{DP}_0 - 10$ (C) $\texttt{Vol} - \texttt{Vol}_0$

FIGURE 11. Convergence histories obtained with the Null Space Optimizer for the optimization problem (4.5) solved without filtering.

where $a(\cdot, \cdot)$ is the bilinear form defined by

$$a(v, v') := \int_D (\gamma^2 \nabla v \cdot \nabla v' + v v') \, \mathrm{d}x,$$

and where the regularization parameter $\gamma$ is set to $\gamma := 0.05$. This classical identification procedure (which traces back at least to [10, 20, 25]) amounts to use a Hilbertian regularization sensitivity filter (sometimes also called "Helmholtz-type filter" [48], but this denomination should be used cautiously since (4.12) is a regularizing problem and not a wave equation) and can be made consistent with first order optimization algorithms [33, 32]. Filtering the Fréchet derivatives of the objective and constraint functions with (4.12), the convergence process becomes stable (Figure 13) and the numerically optimized designs becomes almost devoid of checkerboard patterns (Figure 12).

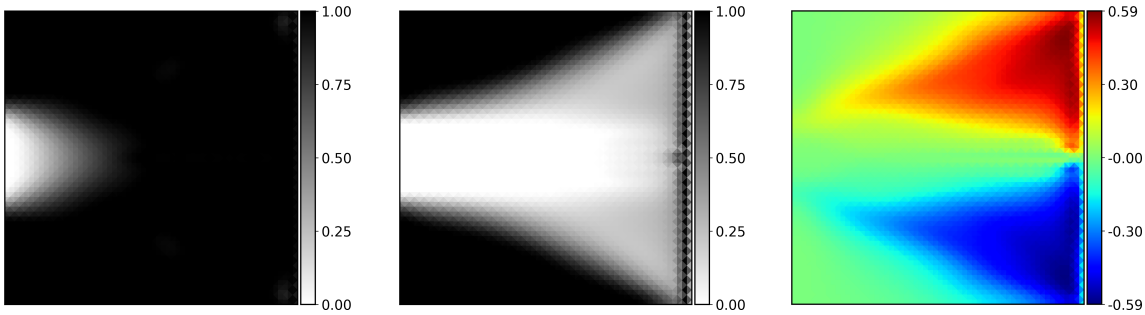


(A) $m_1$ (B) $m_2$ (C) $\theta$

FIGURE 12. Optimized design variables $(m_1, m_2, \theta)$ obtained after 200 iterations of the Null Space Optimizer solving the optimization problem (4.5) with the Hilbertian sensitivity filter (4.12).

Nevertheless, the optimized fields $m_2$ and $\theta$ still incorporates a small layer with checkerboard patterns in the vicinity of the outlet boundary $\Gamma_{\text{out}}$. We conjecture that this effect can be attributed to the fact that

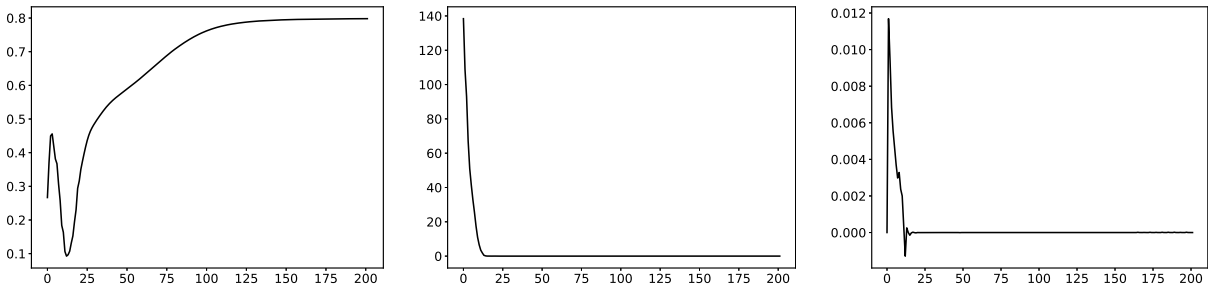

(A) Maximized objective function MINOUT (B) $\texttt{DP}/\texttt{DP}_0 - 10$ (C) $\texttt{Vol} - \texttt{Vol}_0$

FIGURE 13. Convergence histories obtained with the Null Space Optimizer for the optimization problem (4.5) with the Hilbertian sensitivity filter (4.12).

checkerboard designs encourage larger pressure gradients which are favorable to increase the magnitude of the outlet velocity component.

In order to entirely avoid this phenomenon, and to subsequently facilitate the dehomogenization process, we rather solve the following filtered version of the optimization problem (4.5):

$$\max_{\substack{0\le m_1,m_2\le 1\\ \theta\in\mathbb{R}}} \quad \texttt{MINOUT}(\boldsymbol{u}(\widetilde{\widehat{\boldsymbol{m}}})) \qquad s.t. \begin{cases} \texttt{DP}(p(\widetilde{\widehat{\boldsymbol{m}}}) \le 10 \times \texttt{DP}_0 \times \epsilon^{-2}, \\ \texttt{Vol}(\widetilde{\widehat{m}}_1, \widetilde{\widehat{m}}_2) \le \texttt{Vol}_0, \end{cases} \tag{4.13}$$

where $\widetilde{\widehat{\boldsymbol{m}}} = (\widetilde{\widehat{m}}_1, \widetilde{\widehat{m}}_2, \widetilde{\theta})$ contains the filtered design variables. These are obtained by cumulating two density filters.

The first mapping $\rho \mapsto \widehat{\rho}$ is just the Hilbertian regularization filter (4.12) applied to density variables rather than derivatives: it maps $\rho$ to the solution $\widehat{\rho}$ to the variational problem

$$\text{find } \widehat{\rho} \in H^1(D) \text{ such that } \forall v \in H^1(D), \quad \int_D (\gamma^2 \nabla\widehat{\rho}\cdot\nabla v + \widehat{\rho} v)\,\mathrm{d}x = \int_D \rho v\,\mathrm{d}x. \tag{4.14}$$

The regularization parameter is still set to $\gamma = 0.05$ which limits the smallest feature resolved by the fields $\widehat{m}_1$, $\widehat{m}_2$ and $\widehat{\theta}$ to this size. This filter enforces the smoothness of the optimized physical variable even in the vicinity of the outlet, thereby guaranteeing fully checkerboard-free designs.

In order to obtain later on better dehomogenized designs, we use the additional mapping $\widehat{\rho} \mapsto \widetilde{\widehat{\rho}}$ which implements the projection filter of [41]. This filter projects intermediate values of $\widehat{m}_1$ and $\widehat{m}_2$ to either 0 or 1 outside the window $(\eta, 1-\eta)$ for a specified threshold $\eta$. This allows to constrain homogenized designs to feature clearly distinguished porous, solid fluid regions. Following [41], the projection filter is defined by

$$\widetilde{\widehat{m}}_1 := \widehat{m}_1(1 - H(\beta, 1-\eta, \widehat{m}_1))H(\beta, \eta, \widehat{m}_1) + \left(\frac{\beta-1}{\beta} + \frac{\widehat{m}_1}{\beta}\right) H(\beta, 1-\eta, \widehat{m}_1), \tag{4.15}$$

where $H$ is the regularized Heaviside function

$$H(\beta, \eta, \widehat{m}_1) = \frac{\tanh(\beta\eta) + \tanh(\beta(\widehat{m}_1 - \eta))}{\tanh(\beta\eta) + \tanh(\beta(1-\eta))}. \tag{4.16}$$

The parameter $\beta$ controls the sharpness of the approximation of the Heaviside function (the larger is $\beta$ and the sharper is the slope near the origin approximation). In our implementation, we set the parameters to $\eta = 0.1$ and $\beta = 40$. Unlike [41], we do not use a continuation scheme on the parameter $\beta$. The mapping $\widehat{m}_1 \mapsto \widetilde{\widehat{m}}_1$ as well as the smoothed Heaviside function $\widehat{m}_1 \mapsto H(\beta, \eta, \widehat{m}_1)$ of (4.16) are plotted on Figure 14. As $\epsilon$ decreases, the designs feature more and more regularly spaced channels connected to the outlet. The flow is entering the inlet through a single channel which admits a porous transition region before being divided into the multiple channels joining the outlet.

Finally, the sensitivities of the filtered objective function $\boldsymbol{m} \mapsto -\texttt{MINOUT}(\boldsymbol{u}(\widetilde{\widehat{\boldsymbol{m}}}))$ and constraints $\boldsymbol{m} \mapsto \texttt{DP}(p(\widetilde{\widehat{\boldsymbol{m}}}))$ and $\boldsymbol{m} \mapsto \texttt{Vol}(\widetilde{\widehat{m}}_1, \widetilde{\widehat{m}}_2)$ are derived by using the chain rule, which states that the Fréchet derivative of a functional $\boldsymbol{m} \mapsto J(\widetilde{\widehat{\boldsymbol{m}}})$ satisfies

$$\frac{\mathrm{d}J(\widetilde{\widehat{\boldsymbol{m}}})}{\mathrm{d}\boldsymbol{m}} \cdot \delta\boldsymbol{m} = \frac{\mathrm{d}J}{\mathrm{d}\widetilde{\widehat{\boldsymbol{m}}}}(\widetilde{\widehat{\boldsymbol{m}}}) \cdot \frac{\mathrm{d}\widetilde{\widehat{\boldsymbol{m}}}}{\mathrm{d}\widehat{\boldsymbol{m}}} \cdot \frac{\mathrm{d}\widehat{\boldsymbol{m}}}{\mathrm{d}\boldsymbol{m}} \cdot \delta\boldsymbol{m}.$$

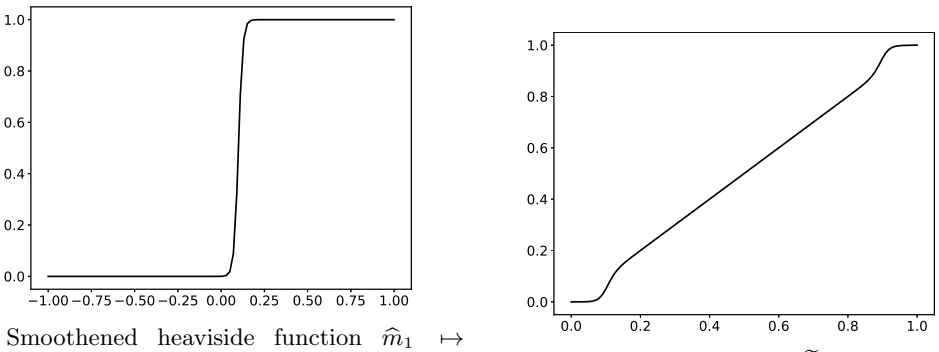


(A) Smoothened heaviside function $\widehat{m}_1 \mapsto H(\beta, \eta, \widehat{m}_1)$ (eq. (4.16)).

(B) Filtering function $\widehat{m}_1 \mapsto \widetilde{\widehat{m}}_1$ (eq. (4.15)).

FIGURE 14. Heaviside and filtering functions used to define the filter $\widehat{m}_1 \mapsto \widetilde{\widehat{m}}_1$ of Section 4.4.

The implementation of this filtering procedure is facilitated by using the decorator `@filtered_optimizable` of the Null Space Optimizer package; see [32].

The numerically optimized physical design variables obtained with this filtering procedure are displayed on Figure 15 (note that we do not further filter the sensitivities with a Hilbertian inner product as in (4.12): we use the standard inner product for identifying Fréchet derivatives to gradients). The obtained designs are now smooth even in the vicinity of the outlet, where $m_1$ is zero and $m_2$ is approximately equal to a constant non-zero value, corresponding physically to regularly spaced outlet channels. Optimization histories with the objective and constraint functions are reported on Figure 16. The optimized design has a performance approximately twice worse than the unfiltered design of Figure 12, but is fully smooth and better suited for dehomogenization.

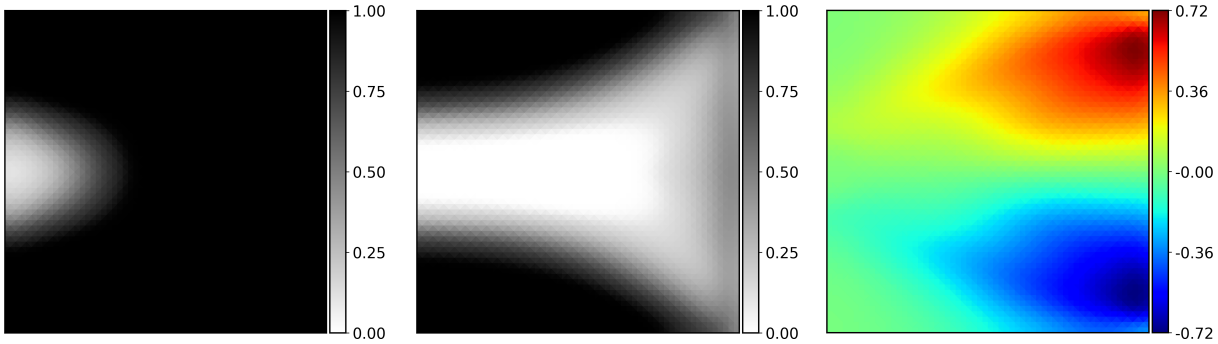


(A) $m_1$ (B) $m_2$ (C) $\theta$

FIGURE 15. Optimized design variables $(m_1, m_2, \theta)$ obtained after 200 iterations of the Null Space Optimizer for solving the optimization problem (4.5) with density filtering.

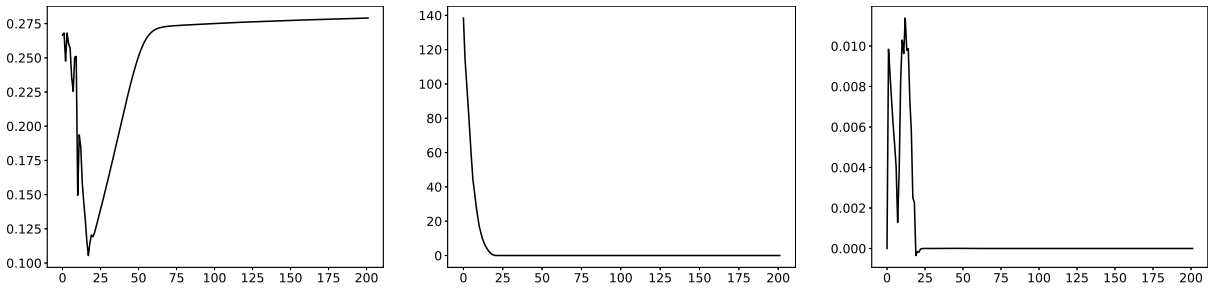


(A) Maximized objective function `MINOUT`

(B) $\texttt{DP}/\texttt{DP}_0 - 10$

(C) $\texttt{Vol} - \texttt{Vol}_0$

FIGURE 16. Convergence histories for the filtered optimization problem (4.5).

## 5. Dehomogenization procedure and numerical results

In this section, we focus on dehomogenizing the homogenized designs obtained with the numerical optimization methodology of the previous Section 4. We employ the dehomogenization procedure from [41] in order

to reconstruct fine scale designs, which we present in Section 5.1. Then in Section 5.2, we validate the performance of the dehomogenized designs by solving the full-scale model. The numerically computed full-scale physical variable enables us additionally to clean dehomogenized designs from spurious channels, a step which we shortly describe in Section 5.3. Finally, the multiscale optimization procedure is tested in Section 5.4 on a second design test case with a different position for the inlet boundary.

### 5.1. **Dehomogenization procedure**

The purpose of the dehomogenization process consists in reconstructing a design with well-defined boundaries from the optimized smooth parameter fields $(\widetilde{\widehat{m}}_1, \widetilde{\widehat{m}}_2, \widehat{\theta})$. Because the orientation vector field $\widehat{\theta}$ shown on Figure 15 is devoid of singularities, we adopt the procedure of [41] which is sufficient for our purpose and simpler to implement than the one of [9].

First, the optimized filtered design variables $(\widetilde{\widehat{m}}_1, \widetilde{\widehat{m}}_2, \widehat{\theta})$ are projected by interpolation from the mesh $\mathcal{T}_{\text{coarse}}$ to a finer mesh $\mathcal{T}_{\text{medium}}$ with resolution $h_{\text{medium}} = 1/200$. In order to avoid the aliasing effect, the interpolated design variables are filtered by solving a variational problem similar to (4.14) with a regularization parameter $\gamma$ set to the minimum edge size of the finer mesh.

Then, we construct a diffeomorphism $\Phi$ satisfying $\nabla\Phi(\Phi^{-1}(x)) \simeq R(\widehat{\theta}(x))$ in order to comply with (4.6). Since the locally periodic porous medium is obtained as the negative subdomain of the level-set function (2.3), we actually construct the inverse $\Phi^{-1}$ of this diffeomorphism on the mesh $\mathcal{T}_{\text{coarse}}$. In what follows, we denote by $(\varphi_1(x), \varphi_2(x))$ the components of $\Phi^{-1}(x)$. Since

$$\nabla\Phi^{-1}(x) = \begin{bmatrix} \nabla\varphi_1(x)^T \\ \nabla\varphi_2(x)^T \end{bmatrix} = (\nabla\Phi(\Phi^{-1}(x)))^{-1} \simeq R(\widehat{\theta})^T = \begin{bmatrix} \cos(\widehat{\theta}) & \sin(\widehat{\theta}) \\ -\sin(\widehat{\theta}) & \cos(\widehat{\theta}) \end{bmatrix},$$

the problem reduces to construct two functions $\varphi_1$ and $\varphi_2$ such that $\nabla\varphi_1 \simeq \boldsymbol{e}_1(\widehat{\theta})$ and $\nabla\varphi_2 \simeq \boldsymbol{e}_2(\widehat{\theta})$, where $\boldsymbol{e}_1(\widehat{\theta})$ and $\boldsymbol{e}_2(\widehat{\theta})$ are the local orientation vectors defined by

$$\boldsymbol{e}_1(\widehat{\theta}) := \begin{bmatrix} \cos(\widehat{\theta}) \\ \sin(\widehat{\theta}) \end{bmatrix}, \qquad \boldsymbol{e}_2(\widehat{\theta}) := \begin{bmatrix} -\sin(\widehat{\theta}) \\ \cos(\widehat{\theta}) \end{bmatrix}.$$

In general, it is not possible to find functions $\varphi_1$ and $\varphi_2$ satisfying exactly $\nabla\varphi_1 = \boldsymbol{e}_1(\widehat{\theta})$ and $\nabla\varphi_2 = \boldsymbol{e}_2(\widehat{\theta})$ without an integrability condition on $\boldsymbol{e}_1(\theta)$ and $\boldsymbol{e}_2(\theta)$. Since we don't impose such integrability condition during the optimization process (see for instance [9, 69] where this approach is considered), we rather implement a compromise between enforcing strictly $\nabla\varphi_1 \cdot \boldsymbol{e}_2(\theta) \simeq 0$ and requiring $\nabla\varphi_1 \simeq \boldsymbol{e}_1(\theta)$. Following [41, 40], we seek $\varphi_1$ as the solution to the following minimization problem:

$$\min_{\varphi_1 \in H^1(D)} \mathcal{I}_1(\varphi_1) := \int_D a(x)|\nabla\varphi_1(x) - \boldsymbol{e}_1(x)|^2 \,\mathrm{d}x + \int_D b(x)|\nabla\varphi_1 \cdot \boldsymbol{e}_2(\theta)|^2 \,\mathrm{d}x, \tag{5.1}$$

where $a(x)$ and $b(x)$ are weights defined by

$$a(x) := \begin{cases} 10^{-3} & \text{if } 1 - \widetilde{\widehat{m}}_1(x)\widetilde{\widehat{m}}_2(x) \geq 1 - \eta, \\ 10^{-3} & \text{if } 1 - \widetilde{\widehat{m}}_1\widetilde{\widehat{m}}_2(x) \leq \eta, \\ 1 & \text{otherwise}, \end{cases} \qquad b(x) := \begin{cases} 0 & \text{if } 1 - \widetilde{\widehat{m}}_1(x)\widetilde{\widehat{m}}_2(x) \geq 1 - \eta, \\ 0 & \text{if } 1 - \widetilde{\widehat{m}}_1\widetilde{\widehat{m}}_2 \leq \eta, \\ 10 & \text{otherwise.} \end{cases}$$

The weight $a(x)$ is set to $10^{-3}$ in regions that are considered as pure fluid or pure solid according to the local volume fraction $1 - \widetilde{\widehat{m}}_1(x)\widetilde{\widehat{m}}_2(x)$ (the use of the small value $10^{-3}$ rather than zero ensures that $\mathcal{I}_1$ is strictly convex). The threshold value determining the limit between porous and solid or pure fluid regions is the same parameter used for defining the density filter $\widehat{\rho} \mapsto \widetilde{\widehat{\rho}}$ in Section 4.4, i.e. it is assigned to $\eta = 0.1$. The weight $b(x)$ is set to 10 in porous regions and zero otherwise.

The minimizer $\varphi_1$ is obtained by solving the first-order optimality condition for the least squares-problem (5.1), i.e. the following variational problem:

find $\varphi_1 \in H^1(D)$ such that $\forall v \in H^1(D)$,

$$\int_D \Big( a(x)\nabla\varphi_1 \cdot \nabla v + b(x)(\nabla\varphi_1 \cdot \boldsymbol{e}_2(\theta))(\nabla v \cdot \boldsymbol{e}_2(\theta)) + 10^{-9}\varphi_1 v \Big) \,\mathrm{d}x = \int_D a(x)\nabla v \cdot \boldsymbol{e}_1(\theta) \,\mathrm{d}x, \tag{5.2}$$

where we have added the bilinear form $\int_D 10^{-9}\varphi_1 v \,\mathrm{d}x$ to fix the constant determining $\varphi_1$. The level-set function $\varphi_2$ is obtained by the identical procedure with $\boldsymbol{e}_1(\theta)$ and $\boldsymbol{e}_2(\theta)$ interchanged. We plot on Figure 17 the optimized orientation field determined by the parameter field $\widehat{\theta}$. On Figure 19 we show on Figure 18 the numerically computed level-set functions $\phi_1$ and $\phi_2$ with the described procedure and the grid corresponding to the underlying diffeomorphism $\Phi$ satisfying $\Phi^{-1} = (\phi_1, \phi_2)$.

Once these two components $(\varphi_1, \varphi_2)$ of the diffeomorphism $\Phi^{-1}$ are computed, we use formula (2.3) with a desired value of $\epsilon$ to reconstruct the medium on a fine mesh with minimum edge size $h_{\text{fine}} = 1/200$. The designs obtained with $\epsilon = 0.05$, $\epsilon = 0.025$ and $\epsilon = 0.0125$ are plotted on Figure 19.

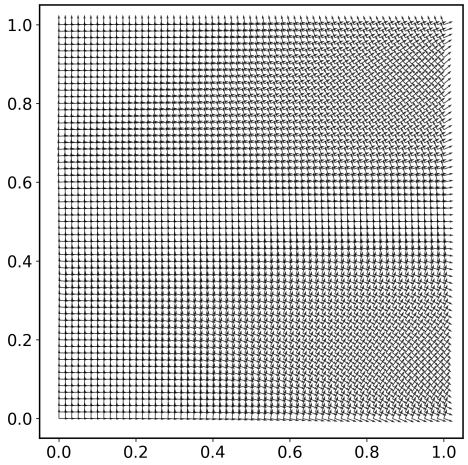


FIGURE 17. Optimized orientation field $(\boldsymbol{e}_1(\widehat{\theta}), \boldsymbol{e}_2(\widehat{\theta}))$.

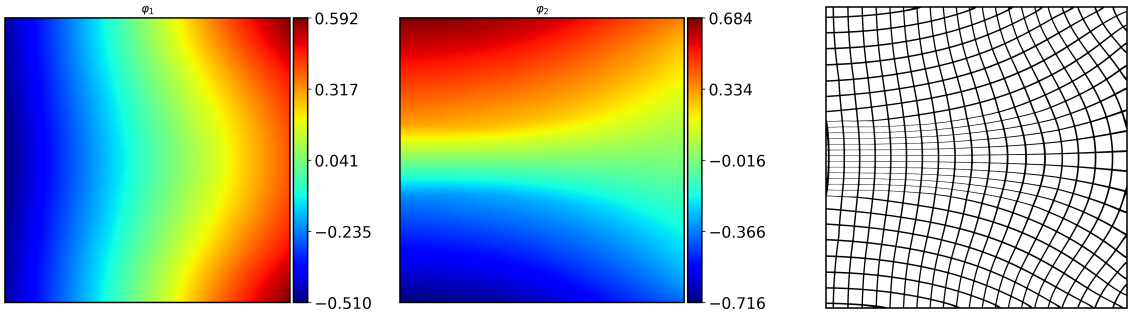


(A) $\varphi_1$ (B) $\varphi_2$ (C) $\Phi$

FIGURE 18. Reconstructed diffeomorphism from the level set functions $\varphi_1$ and $\varphi_2$ with the procedure of Section 5.

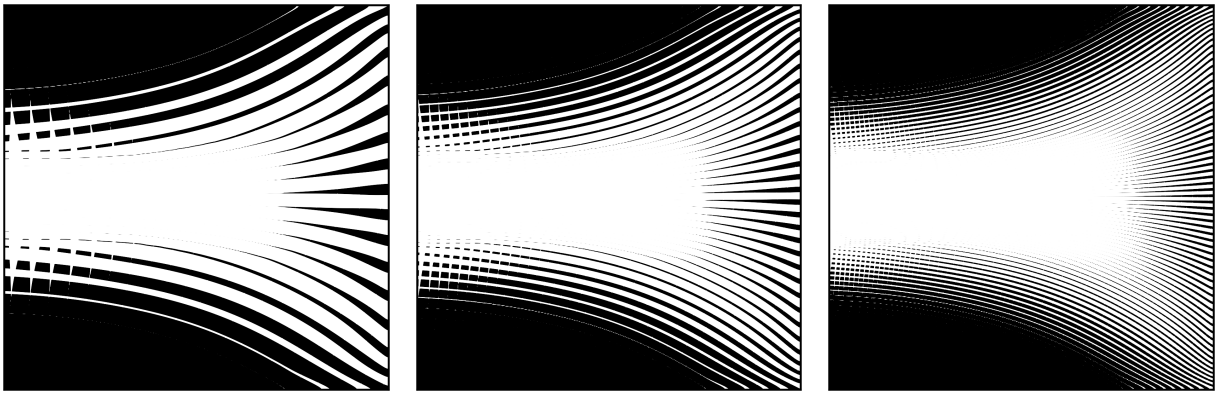

(A) $\epsilon = 0.05$. (B) $\epsilon = 0.025$. (C) $\epsilon = 0.0125$.

FIGURE 19. Dehomogenized designs for various values of $\epsilon$.

### 5.2. **Numerical comparisons with the full-scale model**

In order to assess qualitatively the performance of the proposed designs, we construct a fine mesh $\mathcal{T}_{\text{adapted}}$ adapted to the fluid domain by discretizing the zero isovalue of the level-set function $\rho_\epsilon$ of (2.3) and improving the quality of the mesh by remeshing with the open-source library MMg [24]. We then solve the full-scale model (2.1) on the mesh $\mathcal{T}_{\text{adapted}}$. We do this evaluation for $\epsilon \in \{0.05, 0.025, 0.0125\}$.

We plot the pressure fields on Figure 20 which are compared with the one obtained from the homogenized model (4.1). For this example, the full-scale pressure fields presents rather important deviations with respect to the homogenized pressure field. We then plot on Figure 21 the magnitude of the velocity field expected by

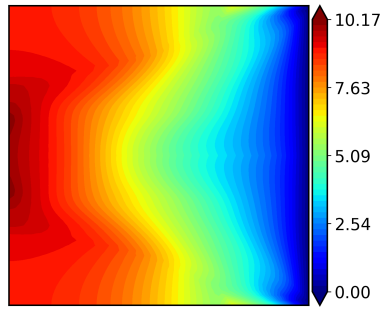


(A) Homogenized model

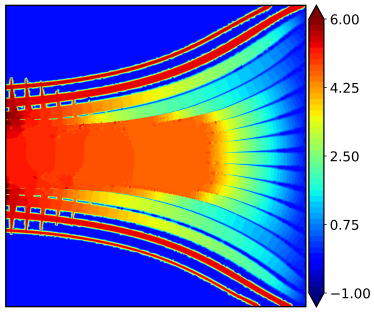


(B) Full-Scale model (2.1) on an adapted mesh.

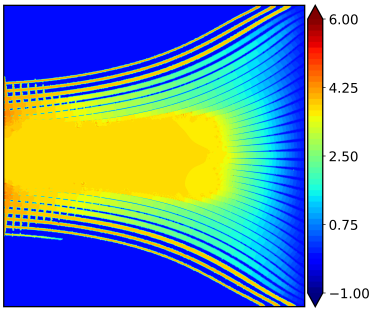


(C) Full-Scale model (2.1) on an adapted mesh.

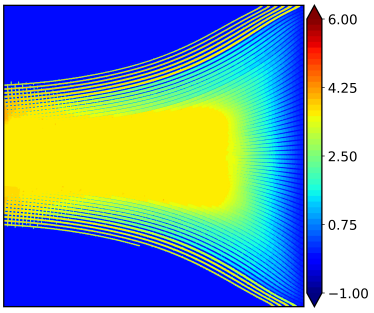


(D) Full-Scale model (2.1) on an adapted mesh.

FIGURE 20. Pressure field obtained by solving the Stokes equation with the homogenized model on $\mathcal{T}_{\text{coarse}}$ and with the full-scale model on a fine mesh $\mathcal{T}_{\text{adapted}}$ adapted to the dehomogenized designs of Figure 19. The magnitude of the pressure fields are scaled by $\epsilon^2$ to enable comparison.

the homogenized model that we compared to those obtained with the full scale model for the three values of $\epsilon$. Here the agreement with the homogenized model is also not perfect.

In order to quantitatively verify whether the goal of enforcing an approximately constant outlet flow has been achieved, we plot on Figure 21b the average mass flow rate $m_i$ on every outlet boundary $\Gamma_{\text{out},i}$, that is

$$m_i = \frac{1}{|\Gamma_{\text{out},i}|} \int_{\Gamma_{\text{out},i}} \boldsymbol{v} \cdot \boldsymbol{n} \, \mathrm{d}\sigma, \tag{5.3}$$

where $\Gamma_{\text{out},i}$ denotes the $i$-th outlet. The horizontal axis corresponds to the $y$ coordinate on the right boundary $\Gamma_{\text{out}}$. As illustrated on this figure, the obtained design fails to achieve a perfectly constant mass flow rate, with outlet flow values distributed between 0.1 and 0.5. Still, the proposed design performs qualitatively well in the sense that a wide portion of the outlet channels computed with the full-scale model achieve outlet velocities larger than the value predicted by the homogenized model. However, the significant quantitative discrepancy highlights the limitations of the proposed homogenized model to accurately capture the physics of the periodically modulated medium. Interestingly, the full scale velocities depicted on Figure 21 seem to converge to a limiting field as $\epsilon \to 0$, suggesting that a better homogenized model could possibly be found.

### 5.3. **Cleaning of dehomogenized designs**

The dehomogenized designs of Figure 19 are not fully satisfying in the sense that they feature channels connected to wall boundaries which do not belong to the outlet. We partially explain this phenomenon by the fact that the wall boundary condition $\boldsymbol{u} \cdot \boldsymbol{n}$ on $\partial D \backslash (\Gamma_{\text{in}} \cup \Gamma_{\text{out}})$ is not enforced exactly by the discrete model, since it is an essential boundary condition. This leads small parts of the wall boundaries featuring small non-vanishing normal velocity components.

Once the velocity field has been computed on a fine mesh, it is rather straightforward to post process these designs to remove channels featuring very small flow motion. Post-processed designs obtained by removing parts of the fluid domain at which the local magnitude of the velocity is smaller than 0.1% than its maximum value are represented on Figure 22. We numerically verified that this post-processing induces minor alterations of the flow profiles.

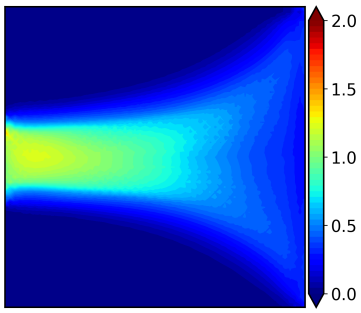


(A) Homogenized model

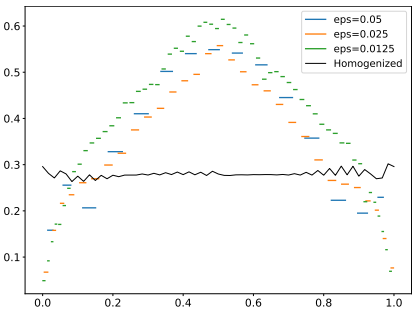


(B) Mean mass flow rates on every outlet channel $\Gamma_{\text{out},i}$ along $\Gamma_{\text{out}}$ (eq. (5.3)). Axis is the $y$ variable on $\Gamma_{\text{out}}$.

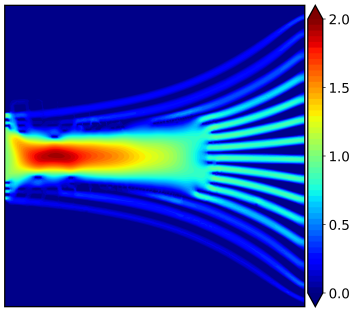


(C) Full-Scale model (2.1) on an adapted mesh.

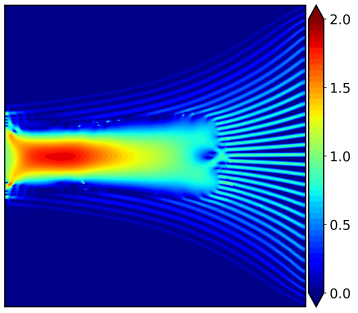


(D) Full-Scale model (2.1) on an adapted mesh.

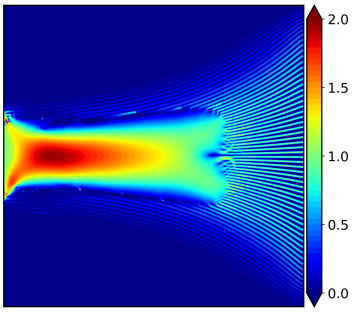


(E) Full-Scale model (2.1) on an adapted mesh.

FIGURE 21. Norm of the velocity field obtained by solving the Stokes equation on a fine mesh discretizing the dehomogenized design of Section 5 with $\epsilon = 0.025$.

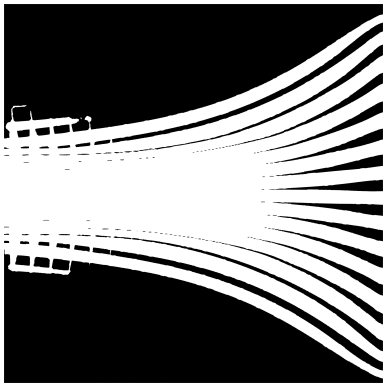

(A) $\epsilon = 0.05$

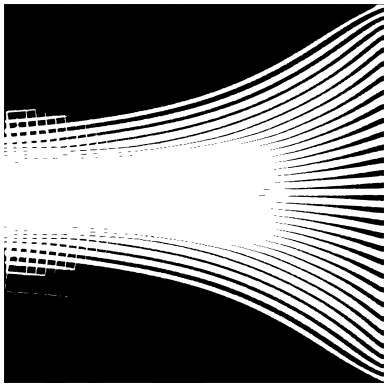

(B) $\epsilon = 0.025$

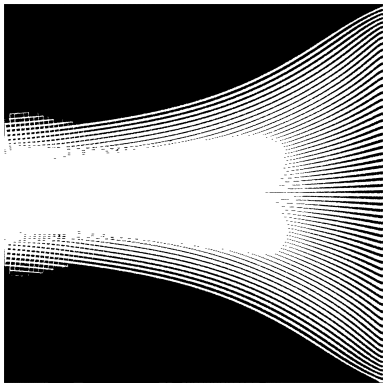

(C) $\epsilon = 0.0125$

FIGURE 22. Post-processed designs obtained by removing channels with very small velocity (compare with Figure 19.

### 5.4. **Multiscale Topology Optimization of a non-symmetric microchannel device**

In this last subsection, we present the results of the previous numerical procedure applied to the design of a microchannel spreading device with an alternative non-symmetric configuration. The physical setting for the design problem is shown on Figure 23: the fluid is entering through a small inlet $\Gamma_{\text{in}}$ of width 0.1 situated on the left of the bottom boundary. For this test case, the pressure constant is set to $\texttt{DP}_0 = 0.5$ and the other parameters are left unchanged. The optimized design variables $(\widehat{\widetilde{m}}_1, \widehat{\widetilde{m}}_2, \widehat{\theta})$ obtained by solving the optimization problem (4.13) on the coarse mesh $\mathcal{T}_{\text{coarse}}$ are shown on Figure 24 and the optimization histories on Figure 25. In this situation, we obtain non-trivial non-symmetric distributions of geometric parameters $\widehat{\widetilde{m}}_1$ and $\widehat{\widetilde{m}}_2$ and orientation $\widehat{\theta}$.

The components $(\varphi_1, \varphi_2)$ of the diffeomorphism $\Phi^{-1}$ reconstructed from on the optimized orientation $\widehat{\theta}$ with the procedure of Section 5 are represented on Figure 26. The inferred dehomogenized designs for $\epsilon \in \{0.05, 0.025, 0.0125\}$ computed on the fine mesh with $N = 600$ are plotted on Figure 27.

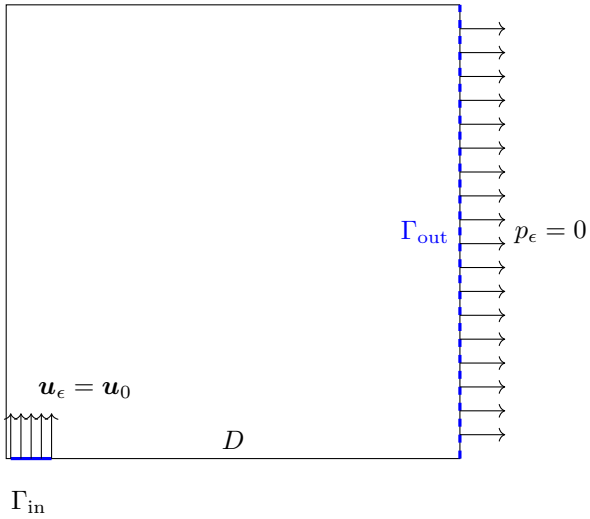


FIGURE 23. Physical domain $D$ with non-symmetric configuration for the inlet and outlet boundaries $\Gamma_{\text{in}}$ and $\Gamma_{\text{out}}$ considered in Section 5.4.

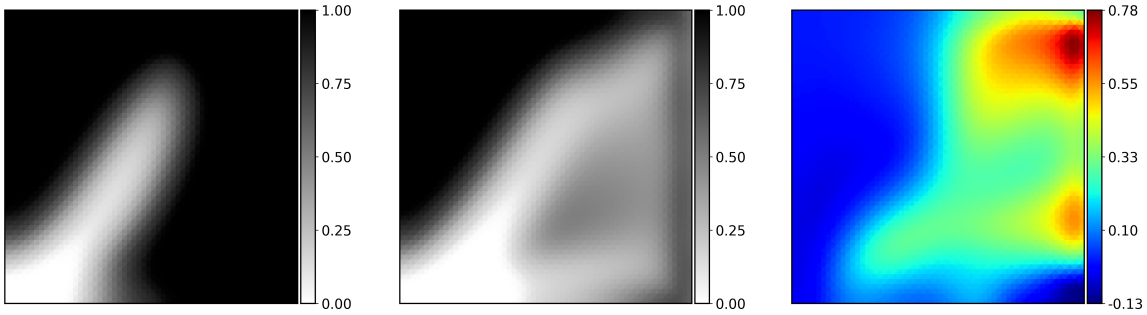


(A) $m_1$ (B) $m_2$ (C) $\theta$

FIGURE 24. Optimized design variables $(m_1, m_2, \theta)$ obtained after 200 iterations of the Null Space Optimizer for solving the optimization problem (4.5) without filtering for the non-symmetric configuration of Section 5.4.

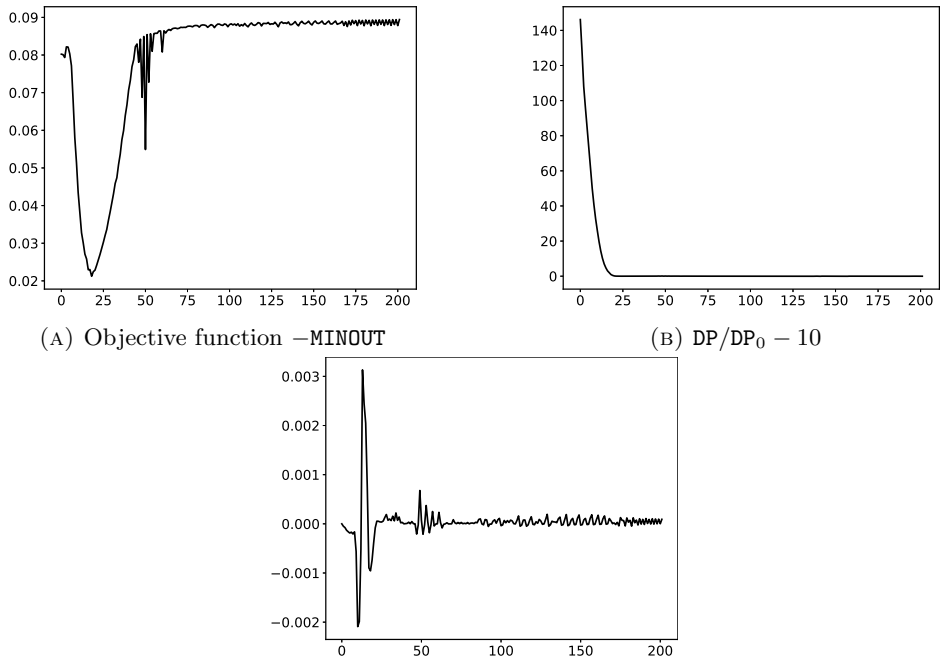


(A) Objective function $-\texttt{MINOUT}$ (B) $\texttt{DP}/\texttt{DP}_0 - 10$

(C) $\texttt{Vol} - \texttt{Vol}_0$

FIGURE 25. Convergence histories for the optimization problem (4.5) for the non-symmetric configuration considered in Section 5.4.

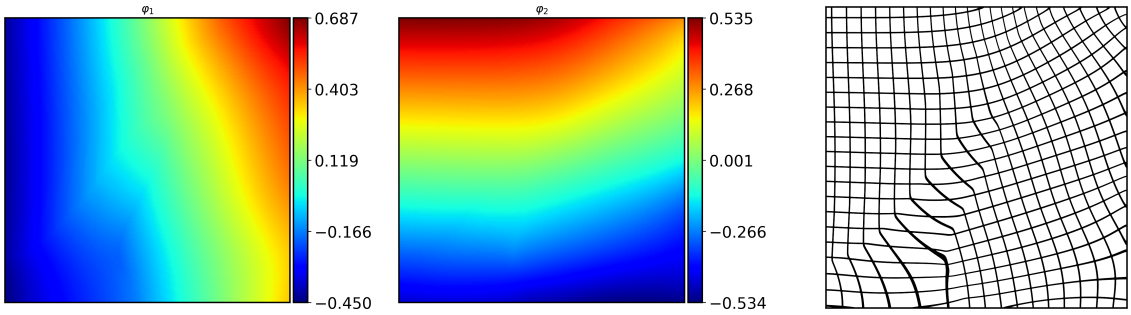


(A) $\varphi_1$ (B) $\varphi_2$ (C) $\Phi$

FIGURE 26. Reconstructed diffeomorphism from the level set functions $\varphi_1$ and $\varphi_2$ with the procedure of Section 5 for the non-symmetric design optimization test case of Section 5.4.

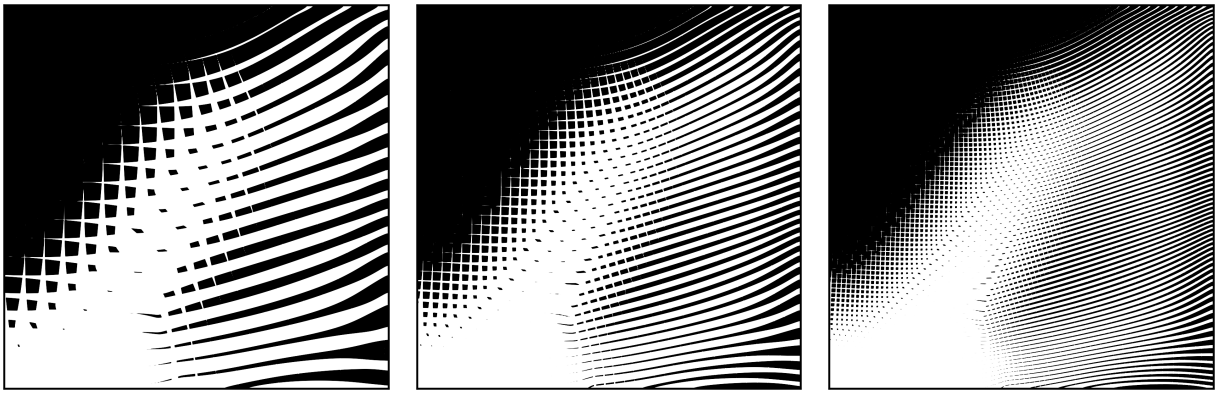

(A) $\epsilon = 0.05$. (B) $\epsilon = 0.025$. (C) $\epsilon = 0.0125$.

FIGURE 27. Dehomogenized designs for various values of $\epsilon$ for the non-symmetric design optimization problem of Section 5.4.

Finally, we evaluate the quality of the proposed designs by solving the full-scale model (2.1) on the fine mesh $\mathcal{T}_{\text{fine}}$. The obtained pressure field and norm of the velocity fields are compared to the solutions to the homogenized model on respectively Figs. 28 and 29. For this test case, the predictions of full-scale and the homogenized model match qualitatively well, a little less for the fine situation $\epsilon = 0.0125$. Looking at the graph of the average mass flow rate $m_i$ at the outlet boundaries $\Gamma_{\text{out},i}$ on Figure 29b (eq. (5.3)), we see that the flow is spread only approximately evenly at the outlet: the design achieve output mass flow rates ranging between 0.15 and 0.25, which is above the value 0.1 obtained from the homogenized model.

Finally, we show on Figure 30 the post-processed designs obtained by removing spurious channels with velocity smaller than 0.1% of its maximum value.

## 6. Conclusion and perspectives

In conclusion, our study is an attempt to pave the way towards unlocking the potential of multiscale topology optimization methods based on asymptotic homogenization for designing intricate fluid systems. In this paper, we raised attention on some challenges that need to be addressed when extending dehomogenization methods from mechanical to fluid models. Using asymptotic analysis, we emphasized the dependency of the homogenized permeability matrix to the local dilation of the underlying locally periodic medium.

We then presented a numerical methodology resting on multiple approximations for solving optimal design problems of two-dimensional systems featuring locally periodic microchannels compatible with the dehomogenization procedure of [41]. Compared to the existing method of Dede et. al. [26], our method is as rigorously as possible based on two-scale asymptotic homogenization and could extend easily to arbitrarily complex unit cell patterns by solving the cell problem (3.2) with a different hole shape $T$, and then by adapting the tiling procedure, see e.g. [66]. In contrast, the variability of admissible Turing patterns seems currently rather limited to stripe or spot shapes whose geometry is controlled by the convection-reaction parameters [45]. In comparison with the alternative method of [53, 54] also based on periodic homogenization, the proposed dehomogenization method is able to generate designs that are not restricted to periodic arrangements of micropillar arrays with a locally varying pattern. We note that in the latter works, the pattern can be chosen within a variety of unit cells (which theoretically could also be considered in the present framework), but these cells are projected on a (nondeformed) cartesian grid, limiting the range and the complexity of achievable designs.

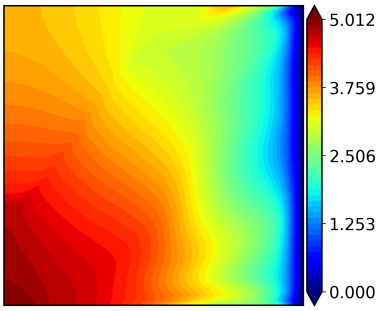


(A) Homogenized model

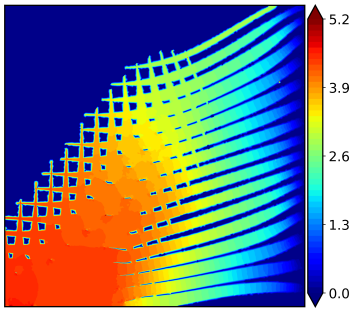


(B) Full-Scale model (2.1) on an adapted mesh, $\epsilon = 0.05$.

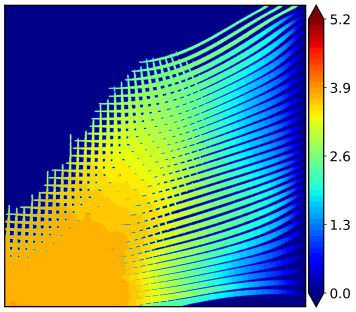


(C) Full-Scale model (2.1) on an adapted mesh, $\epsilon = 0.025$.

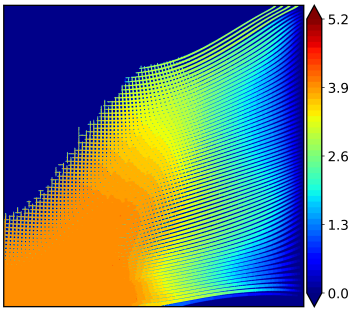


(D) Full-Scale model (2.1) on an adapted mesh, $\epsilon = 0.0125$.

FIGURE 28. Pressure field obtained by solving the Stokes equation on a fine mesh discretizing the dehomogenized design of Section 5 with $\epsilon = 0.025$ for the non-symmetric configuration of Section 5.4.

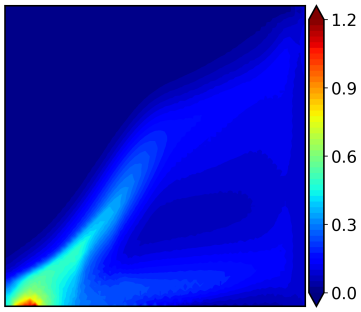


(A) Homogenized model

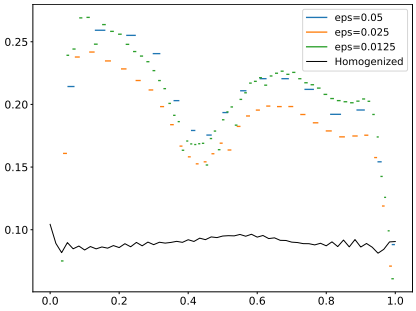


(B) Mean mass flow rates on every outlet channel $\Gamma_{\text{out},i}$ along $\Gamma_{\text{out}}$ (eq. (5.3)). Axis is the $y$ variable on $\Gamma_{\text{out}}$.

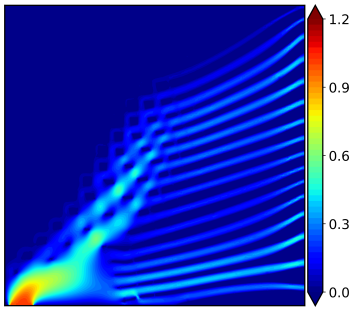


(C) Full-Scale model (2.1) on an adapted mesh, $\epsilon = 0.05$.

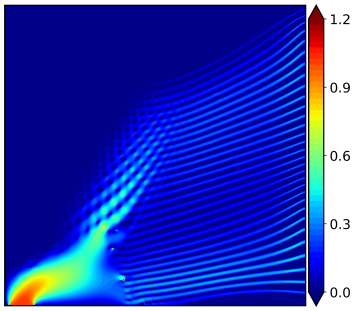


(D) Full-Scale model (2.1) on an adapted mesh, $\epsilon = 0.025$.

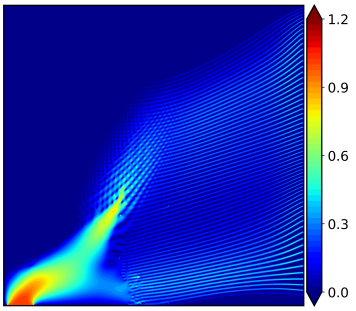


(E) Full-Scale model (2.1) on an adapted mesh, $\epsilon = 0.0125$.

FIGURE 29. Norm of the velocity field obtained by solving the Stokes equation on a fine mesh discretizing the dehomogenized design of Section 5 for the non-symmetric test case of Section 5.4.

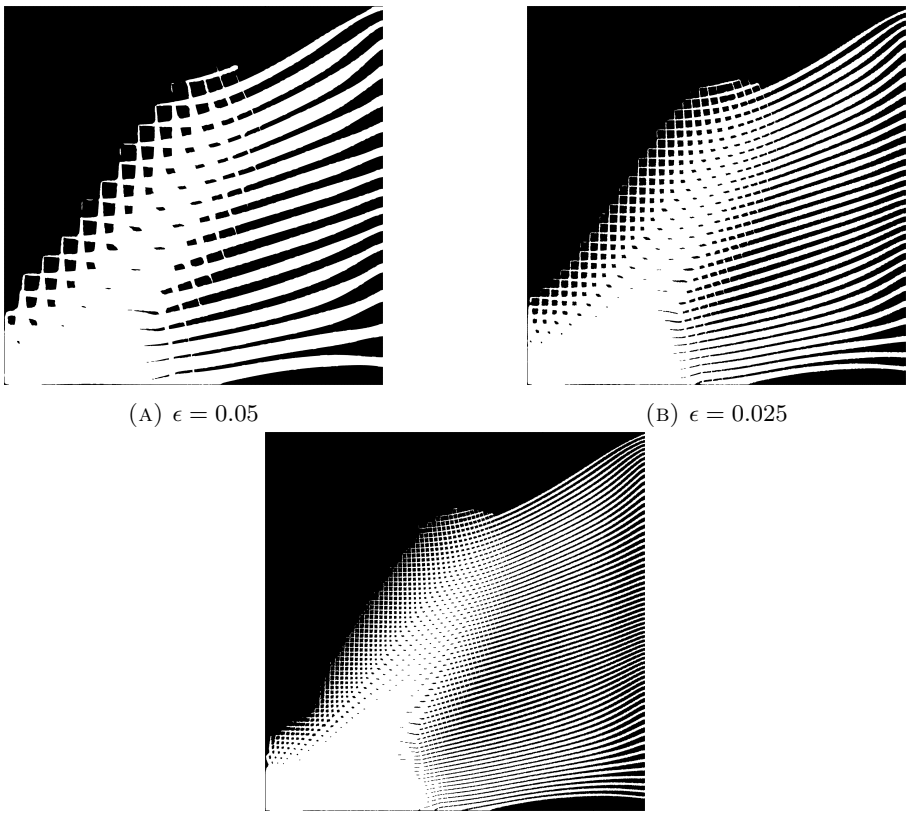

(A) $\epsilon = 0.05$ (B) $\epsilon = 0.025$

(C) $\epsilon = 0.0125$

FIGURE 30. Post-processed designs obtained by removing channels with very small velocity.

The extension of the method to three-dimensional problems would be in principle feasible with the 3D dehomogenization procedure of [42], without theoretical difficulties as long as no singularities of the orientation field is involved. However, the method would rest on the same approximations.

Still, the numerical results of Section 5 highlights several limitations of the method. First, the mapping used to deform the periodic cell in dehomogenization methods is approximately conformal Section 5, which is naturally adapted to compliance minimization problems featuring bars crossing perpendicularly, but this must obviously be less performant for the case of microchannels whose junctions need not to be aligned according to square angles. Furthermore, the proposed approach based on the Darcy system (4.3) fails to capture the velocity and pressure field accurately. In contrast, a rather good agreement between the full-scale and the homogenized model is reported in the alternative dehomogenization method of [53, 26, 68]. More accurate homogenized models should be sought to minimize physical discrepancies between the homogenized and the dehomogenized medium; for instance, a Brinkman equation featuring the inverse of the homogenized Darcy tensor as porosity coefficient is used in [53]. Future investigations could therefore seek to devise methods able to handle non-conformal mappings, and foreseeing improved homogenized descriptions of porous media. Finally, devising an efficient and consistent cleaning procedure for obtaining designs devoid of channels not connected to the outlet or the inlet remains an import open issue that needs to be addressed in future works.

## REFERENCES


[1] FreeFEM website. https://freefem.org/.

[2] ALEXANDRE, R. Homogenisation and $\theta$ — 2 convergence. *Proceedings of the Royal Society of Edinburgh Section A: Mathematics 127*, 3 (Jan. 1997), 441–455.

[3] ALLAIRE, G. Continuity of the Darcy's law in the low-volume fraction limit. *Annali della Scuola Normale Superiore di Pisa-Classe di Scienze 18*, 4 (1991), 475–499.

[4] ALLAIRE, G. Homogenization of the Navier-Stokes equations in open sets perforated with tiny holes I. Abstract framework, a volume distribution of holes. *Archive for Rational Mechanics and Analysis 113*, 3 (Sept. 1991), 209–259.

[5] ALLAIRE, G., AND AMAR, M. Boundary layer tails in periodic homogenization. *ESAIM: Control, Optimisation and Calculus of Variations 4* (1999), 209–243.

[6] ALLAIRE, G., BAL, G., AND SIESS, V. Homogenization and localization in locally periodic transport. *ESAIM: Control, Optimisation and Calculus of Variations 8* (Jan. 2002), 1–30.

[7] ALLAIRE, G., BONNETIER, E., FRANCFORT, G., AND JOUVE, F. Shape optimization by the homogenization method. *Numerische Mathematik 76*, 1 (Mar. 1997), 27–68.

[8] Allaire, G., Dapogny, C., and Jouve, F. Chapter 1 - Shape and topology optimization. In *Handbook of Numerical Analysis*, A. Bonito and R. H. Nochetto, Eds., vol. 22 of *Geometric Partial Differential Equations - Part II*. Elsevier, Jan. 2021, pp. 1–132.

[9] Allaire, G., Geoffroy-Donders, P., and Pantz, O. Topology optimization of modulated and oriented periodic microstructures by the homogenization method. *Computers & Mathematics with Applications 78*, 7 (Oct. 2019), 2197–2229.

[10] Azegami, H., and Wu, Z. C. Domain Optimization Analysis in Linear Elastic Problems : Approach Using Traction Method. *JSME international journal. Ser. A, Mechanics and material engineering 39*, 2 (1996), 272–278.

[11] Balay, S., Gropp, W. D., McInnes, L. C., and Smith, B. F. Efficient management of parallelism in object oriented numerical software libraries. In *Modern Software Tools in Scientific Computing* (1997), E. Arge, A. M. Bruaset, and H. P. Langtangen, Eds., Birkhäuser Press, pp. 163–202.

[12] Barber, R. W., and Emerson, D. R. Optimal design of microfluidic networks using biologically inspired principles. *Microfluidics and Nanofluidics 4*, 3 (Mar. 2008), 179–191.

[13] Bendsoe, M. P., and Sigmund, O. *Topology Optimization: Theory, Methods, and Applications*. Springer Science & Business Media, Dec. 2003.

[14] Blanc, F., and Nazarov, S. A. Asymptotics of solutions to the poisson problem in a perforated domain with corners. *Journal de Mathématiques Pures et Appliquées 76*, 10 (Dec. 1997), 893–911.

[15] Blanc, X., and Wolf, S. Homogenization of the Poisson equation in a non-periodically perforated domain, Sept. 2020.

[16] Bourgeat, A., Marušić-Paloka, E., and Mikelić, A. Weak nonlinear corrections for darcy's law. *Mathematical Models and Methods in Applied Sciences 06*, 08 (Dec. 1996), 1143–1155.

[17] Briane, M. Three models of non periodic fibrous materials obtained by homogenization. *ESAIM: Mathematical Modelling and Numerical Analysis 27*, 6 (1993), 759–775.

[18] Briane, M. Homogenization of a non-periodic material. *Journal de Mathématiques Pures et Appliquées. Neuvième Série 73*, 1 (1994), 47–66.

[19] Buckinx, G., and Baelmans, M. Macro-scale heat transfer in periodically developed flow through isothermal solids. *Journal of Fluid Mechanics 780* (Oct. 2015), 274–298.

[20] Burger, M. A framework for the construction of level set methods for shape optimization and reconstruction. *Interfaces and Free Boundaries 5*, 3 (Sept. 2003), 301–329.

[21] Chechkin, G. A., and Piatnitski, A. L. Homogenization of Boundary-Value Problem in a Locally Periodic Perforated Domain. *Applicable Analysis 71*, 1-4 (Dec. 1998), 215–235.

[22] Chenais, D., Mascarenhas, M. L., and Trabucho, L. On the optimization of non periodic homogenized microstructures. *ESAIM: Mathematical Modelling and Numerical Analysis 31*, 5 (1997), 559–597.

[23] Conca, C., Murat, F., and Pironneau, O. The Stokes and Navier-Stokes equations with boundary conditions involving the pressure. *Japanese journal of mathematics. New series 20*, 2 (1994), 279–318.

[24] Dapogny, C., Dobrzynski, C., and Frey, P. Three-dimensional adaptive domain remeshing, implicit domain meshing, and applications to free and moving boundary problems. *Journal of Computational Physics* (Apr. 2014).

[25] de Gournay, F. Velocity Extension for the Level-set Method and Multiple Eigenvalues in Shape Optimization. *SIAM Journal on Control and Optimization 45*, 1 (Jan. 2006), 343–367.

[26] Dede, E. M., Zhou, Y., and Nomura, T. Inverse design of microchannel fluid flow networks using Turing pattern dehomogenization. *Structural and Multidisciplinary Optimization 62*, 4 (2020), 2203–2210.

[27] Dede, E. M., Zhou, Y., Tambo, T., Zhou, F., Lohan, D. J., and Nomura, T. Measurement of low Reynolds number flow emanating from a Turing pattern microchannel array using a modified Bernoulli equation technique. *Experimental Thermal and Fluid Science 139* (Nov. 2022), 110722.

[28] Doubrovski, Z., Verlinden, J. C., and Geraedts, J. M. P. Optimal Design for Additive Manufacturing: Opportunities and Challenges. In *ASME 2011 International Design Engineering Technical Conferences and Computers and Information in Engineering Conference* (June 2012), American Society of Mechanical Engineers Digital Collection, pp. 635–646.

[29] Fahrenkopf, M. A., Ydstie, B. E., Mukherjee, T., and Schneider, J. W. Optimal Design of Microfluidic Devices for Rapid DNA Separations. *IFAC Proceedings Volumes 46*, 31 (Jan. 2013), 137–142.

[30] Feppon, F. Null space optimizer. https://gitlab.com/florian.feppon/null-space-optimizer/, 2020.

[31] Feppon, F. High Order Homogenization of the Stokes System in a Periodic Porous Medium. *SIAM Journal on Mathematical Analysis 53*, 3 (Jan. 2021), 2890–2924.

[32] Feppon, F. Density based topology optimization with the Null Space Optimizer: A tutorial and a comparison. *HAL preprint hal-04155507* (2023).

[33] Feppon, F., Allaire, G., and Dapogny, C. Null space gradient flows for constrained optimization with applications to shape optimization. *ESAIM: Control, Optimisation and Calculus of Variations* (2020), 90.

[34] Feppon, F., and Ammari, H. High Order Topological Asymptotics: Reconciling Layer Potentials and Compound Asymptotic Expansions. *Multiscale Modeling & Simulation 20*, 3 (Sept. 2022), 957–1001.

[35] Feppon, F., and Ammari, H. Homogenization of sound-soft and high-contrast acoustic metamaterials in subcritical regimes. *ESAIM: Mathematical Modelling and Numerical Analysis 57*, 2 (Mar. 2023), 491–543.

[36] Feppon, F., and Jing, W. High order homogenized Stokes models capture all three regimes. *SIAM Journal on Mathematical Analysis 54*, 4 (2022), 5013–5040.

[37] Garnier, D.-H., Schmidt, M.-P., and Rohmer, D. Growth of oriented orthotropic structures with reaction/diffusion. *Structural and Multidisciplinary Optimization 65*, 11 (Nov. 2022), 327.

[38] Gérard-Varet, D., and Masmoudi, N. Homogenization and boundary layers. *Acta Mathematica 209*, 1 (2012), 133–178.

[39] Gloria, A., and Otto, F. An optimal variance estimate in stochastic homogenization of discrete elliptic equations. *The Annals of Probability 39*, 3 (May 2011), 779–856.

[40] Groen, J. *Multi-Scale Design Methods for Topology Optimization*. PhD thesis, Technical University of Denmark, 2018.

[41] Groen, J. P., and Sigmund, O. Homogenization-based topology optimization for high-resolution manufacturable microstructures. *International Journal for Numerical Methods in Engineering 113*, 8 (2018), 1148–1163.

[42] Groen, J. P., Stutz, F. C., Aage, N., Bærentzen, J. A., and Sigmund, O. De-homogenization of optimal multi-scale 3D topologies. *Computer Methods in Applied Mechanics and Engineering 364* (2020), 112979.

[43] Groen, J. P., Wu, J., and Sigmund, O. Homogenization-based stiffness optimization and projection of 2D coated structures with orthotropic infill. *Computer Methods in Applied Mechanics and Engineering 349* (June 2019), 722–742.

[44] Guest, J. K., and Prévost, J. H. Design of maximum permeability material structures. *Computer Methods in Applied Mechanics and Engineering 196*, 4 (Jan. 2007), 1006–1017.
[45] Hankins, S. N., Zhou, Y., Lohan, D. J., and Dede, E. M. Generative design of large-scale fluid flow structures via steady-state diffusion-based dehomogenization. *Scientific Reports 13*, 1 (Sept. 2023), 1–14.
[46] Hecht, F. New development in FreeFem++. *Journal of numerical mathematics 20*, 3-4 (2012), 251–266.
[47] John, F. Rotation and strain. *Communications on Pure and Applied Mathematics 14*, 3 (1961), 391–413.
[48] Lazarov, B. S., and Sigmund, O. Filters in topology optimization based on Helmholtz-type differential equations. *International Journal for Numerical Methods in Engineering 86*, 6 (2011), 765–781.
[49] Lerou, J. J., Tonkovich, A. L., Silva, L., Perry, S., and McDaniel, J. Microchannel reactor architecture enables greener processes. *Chemical Engineering Science 65*, 1 (Jan. 2010), 380–385.
[50] Marusic-Paloka, E., and Mikelic, A. An Error Estimate for Correctors in the Homogenization of the Stokes and the Navier-Stokes Equations in a Porous Medium. *Bollettino della Unione Matematica Italiana A* (1996).
[51] Milton, G. W. *The Theory of Composites*. Cambridge Monographs on Applied and Computational Mathematics. Cambridge University Press, Cambridge, 2002.
[52] Ozguc, S., Pan, L., and Weibel, J. A. Topology optimization of microchannel heat sinks using a homogenization approach. *International Journal of Heat and Mass Transfer 169* (Apr. 2021), 120896.
[53] Padhy, R. K., Chandrasekhar, A., and Suresh, K. FluTO: Graded Multiscale Fluid Topology Optimization using Neural Networks. *arXiv preprint arXiv:2209.08168* (Sept. 2022).
[54] Padhy, R. K., Suresh, K., and Chandrasekhar, A. TOMAS: Topology Optimization of Multiscale Fluid Devices using Variational Autoencoders and Super-Shapes, Sept. 2023.
[55] Piovesan, A. *Computational Modelling and Engineering of Fluid Flow in 3D- Printed Microfluidic Lab-on-Chips*. PhD thesis, KU Leuven, 2022.
[56] Ptashnyk, M. Two-Scale Convergence for Locally Periodic Microstructures and Homogenization of Plywood Structures. *Multiscale Modeling & Simulation 11*, 1 (Jan. 2013), 92–117.
[57] Sabau, A. S., Bejan, A., Brownell, D., Gluesenkamp, K., Murphy, B., List, F., Carver, K., Schaich, C. R., and Klett, J. W. Design, additive manufacturing, and performance of heat exchanger with a novel flow-path architecture. *Applied Thermal Engineering 180* (Nov. 2020), 115775.
[58] Sanchez-Palencia, E. Fluid flow in porous media. In *Non-Homogeneous Media and Vibration Theory*, Lecture Notes in Physics. Springer, Berlin, Heidelberg, 1980, pp. 129–157.
[59] Sigmund, O., and Petersson, J. Numerical instabilities in topology optimization: A survey on procedures dealing with checkerboards, mesh-dependencies and local minima. *Structural optimization 16*, 1 (Aug. 1998), 68–75.
[60] Sun, H., Jia, Y., Dong, H., Dong, D., and Zheng, J. Combining additive manufacturing with microfluidics: An emerging method for developing novel organs-on-chips. *Current Opinion in Chemical Engineering 28* (June 2020), 1–9.
[61] Vyatskikh, A., Delalande, S., Kudo, A., Zhang, X., Portela, C. M., and Greer, J. R. Additive manufacturing of 3D nano-architected metals. *Nature Communications 9*, 1 (Feb. 2018), 593.
[62] Wang, L., Liu, Z., Da, D., Chan, Y.-C., Chen, W., and Zhu, P. Generalized de-homogenization via sawtooth-function-based mapping and its demonstration on data-driven frequency response optimization. *Computer Methods in Applied Mechanics and Engineering 395* (2022), 114967.
[63] Wu, C. Q., Yang, C., Xiao, Q., Ke, H. B., and Xu, H. J. Topology optimization of porous solid structures for heat transfer and flow channels in reactors with fluid-solid reaction coupling. *International Journal of Thermal Sciences 181* (Nov. 2022), 107771.
[64] Wu, J., Sigmund, O., and Groen, J. P. Topology optimization of multi-scale structures: A review. *Structural and Multidisciplinary Optimization 63*, 3 (2021), 1455–1480.
[65] Wu, T. *Topology Optimization of Multiscale Structures Coupling Fluid, Thermal and Mechanical Analysis*. Thesis, Purdue University Graduate School, June 2019.
[66] Xue, D., Zhu, Y., and Guo, X. Generation of smoothly-varying infill configurations from a continuous menu of cell patterns and the asymptotic analysis of its mechanical behaviour. *Computer Methods in Applied Mechanics and Engineering 366* (July 2020), 113037.
[67] Zhao, X., Zhou, M., Sigmund, O., and Andreasen, C. S. A "poor man's approach" to topology optimization of cooling channels based on a Darcy flow model. *International Journal of Heat and Mass Transfer 116* (Jan. 2018), 1108–1123.
[68] Zhou, Y., Lohan, D. J., Zhou, F., Nomura, T., and Dede, E. M. Inverse design of microreactor flow fields through anisotropic porous media optimization and dehomogenization. *Chemical Engineering Journal 435* (2022), 134587.
[69] Zhu, Y., Li, S., Du, Z., Liu, C., Guo, X., and Zhang, W. A novel asymptotic-analysis-based homogenisation approach towards fast design of infill graded microstructures. *Journal of the Mechanics and Physics of Solids 124* (Mar. 2019), 612–633.

## Appendix A. Exact description of the deformed locally periodic domain

It is possible to give an exact description of the geometrically modulated periodic domain $\Omega_\epsilon$ of Section 2.2, characterized by the implicit function $\rho_\epsilon$ of (2.3). To our knowledge, this description has not been investigated in previous works but is of interest as it offers a refined understanding of this set.

Let $x(\boldsymbol{t}, \epsilon, \boldsymbol{s})$ be the implicit function satisfying

$$F(x(\boldsymbol{t}, \epsilon, \boldsymbol{s}), \boldsymbol{t}, \epsilon, \boldsymbol{s}) = 0 \text{ where } F(x, \boldsymbol{t}, \epsilon, \boldsymbol{s}) = \Phi^{-1}(x) - \boldsymbol{t} - \epsilon \boldsymbol{s} \odot \boldsymbol{m}(x)$$

where $\odot$ denotes the coefficient-wise multiplication: $\boldsymbol{s} \odot \boldsymbol{m}(x) = (s_1 m_1(x), s_2 m_2(x))$. The existence and smoothness of the function $x(\boldsymbol{t}, \epsilon, s)$ is guaranteed by the the implicit function theorem for small values of $\epsilon$, $\boldsymbol{t} \in \mathbb{R}^2$ and $s \in (-1/2, 1/2)^2$. The reader can then verify that the negative subdomain of $\rho_\epsilon$ is

$$\{(x_1, x_2) \in \mathbb{R}^2 \,|\, \rho_\epsilon(x_1, x_2) < 0\} = \mathbb{R}^2 \backslash \bigcup_{\boldsymbol{n} \in \mathbb{Z}^2} F_{\boldsymbol{n}\epsilon, \epsilon}((-1/2, -1/2)^2) \text{ where } F_{\boldsymbol{n}\epsilon, \epsilon}(\boldsymbol{s}) = x(\boldsymbol{n}\epsilon, \epsilon, \boldsymbol{s}). \tag{A.1}$$

In other words, $\Omega_\epsilon$ (which is the intersection of this set with $D$) is obtained by removing from $D$ the many small obstacles $F_{\boldsymbol{n}\epsilon,\epsilon}((-1/2,1/2)^2)$ for all possible $\boldsymbol{n}\in\mathbb{Z}^2$.

The obstacle $F_{\boldsymbol{n}\epsilon}((-1/2,1/2)^2)$ is at first order a rectangle of size $m_1(x)\times m_2(x)$ centered around the point $x=\Phi(\boldsymbol{n}\epsilon)$. To be convinced of this fact, the computation of the leading asymptotic expansion of the function $F_{\boldsymbol{n}\epsilon,\epsilon}$ as $\epsilon\to 0$ yields

$$F_{\boldsymbol{n}\epsilon,\epsilon}(\boldsymbol{s}) = x(\boldsymbol{n}\epsilon,\epsilon,\boldsymbol{s}) = \Phi(\boldsymbol{n}\epsilon) + \epsilon\nabla\Phi(\boldsymbol{n}\epsilon)(\boldsymbol{s}\odot\boldsymbol{m}(\Phi(\boldsymbol{n}\epsilon))) + O(\epsilon^2). \tag{A.2}$$

Thus, $F_{\boldsymbol{n}\epsilon,\epsilon}(P)$ is at first order the stretched rectangle $\epsilon\nabla\Phi(\boldsymbol{n}\epsilon)T(\boldsymbol{m})$ of width and height $m_1(\Phi(\boldsymbol{n}\epsilon))$ and $m_2(\Phi(\boldsymbol{n}\epsilon))$, centered around the point $x=\Phi(\boldsymbol{n}\epsilon)$.

Finally, let us justify why the volume functional $\texttt{Vol}(m_1,m_2)=\int_D(1-m_1m_2)\,\mathrm{d}x$ is a consistent approximation of the fluid volume $|\Omega_\epsilon|$. In view of (A.1) and (A.2), the following approximation holds:

$$\begin{aligned}|\Omega_\epsilon| \simeq |D| - \sum_{\boldsymbol{n}\in\mathbb{Z},\,\boldsymbol{n}\epsilon\in D}\epsilon^2 m_1(\Phi(\boldsymbol{n}\epsilon))m_2(\Phi(\boldsymbol{n}\epsilon))|\nabla\Phi(\boldsymbol{n}\epsilon)| &\simeq |D| - \int_{\Phi^{-1}(D)} m_1(\Phi(X))m_2(\Phi(X))|\nabla\Phi|\,\mathrm{d}X\\ &= \int_D (1-m_1(x)m_2(x))\,\mathrm{d}x,\end{aligned}$$

which is the desired result. We note that the formula is valid even for nonconformal mappings $\Phi$.

## Appendix B. Proofs of homogenization theorems on deformed periodic domains

This appendix is dedicated to the proof of the homogenization results of Section 3. The notation conventions of this part are those of Section 3. Throughout this part, we use the Einstein summation convention on repeated indices. Furthermore, in order to make the notation lighter, we omit the dependency to $m_1$ and $m_2$ when referring to the solid obstacle or the fluid component in the unit cell, i.e. $Y\equiv Y(m_1,m_2)$ and $T\equiv T(m_1,m_2)$. In any case, the results presented here are true if the solid inclusion is replaced with any smooth simply connected set, and the results would extend without difficulty to the three-dimensional setting.

### B.1. Proof of Proposition 3.1

We prove the result thanks to two intermediate propositions. First, we introduce a cell problem in the (non-stretched) unit cell $Y=P\backslash T$. For any $x\in\Phi(D)$, let us denote by $(\widehat{\boldsymbol{\mathcal{X}}}_j(x,\cdot),\widehat{\alpha}_j(x,\cdot))_{1\le j\le d}$ the solution to the cell problem

$$\begin{cases} -\mathrm{div}_y(A(x)\nabla_y\widehat{\boldsymbol{\mathcal{X}}}_j(x,y)) + (\nabla\Phi^{-1}(x))^T\nabla_y\widehat{\alpha}_j(x,y) = \boldsymbol{e}_j, & \forall y\in Y,\\ \mathrm{div}_y(\nabla\Phi^{-1}(x)\widehat{\boldsymbol{\mathcal{X}}}_j(x,y)) = 0, & \forall y\in Y,\\ \displaystyle\int_Y \widehat{\alpha}_j(x,y)\,\mathrm{d}y = 0,\\ \widehat{\boldsymbol{\mathcal{X}}}_j(x,\cdot) = 0 \quad \text{on } \partial Y,\\ \widehat{\boldsymbol{\mathcal{X}}}_j(x,\cdot) \text{ is } P\text{–periodic}, \end{cases} \tag{B.1}$$

where $A(x)$ is the fourth order tensor defined by

$$A(x)\xi := \xi\nabla\Phi^{-1}(x)(\nabla\Phi^{-1}(x))^T \text{ for all } 2\times 2 \text{ matrix } \xi.$$

The cell-problem (B.1) is an elliptic, symmetric, problem in $y$ that is well-posed for every $x\in\Phi(D)$ owing to the Lax-Milgram theorem, noting that the matrices $A(x)$ and $\nabla\Phi^{-1}(x)$ are constant in $y$. The symmetry of the system (B.1) comes from the fact that the operator $\widehat{\alpha}\mapsto(\nabla\Phi^{-1}(x))^T\nabla_y\widehat{\alpha}$ is the transpose of the operator $\widehat{\boldsymbol{\mathcal{X}}}\mapsto\mathrm{div}_y(\nabla\Phi^{-1}(x)\widehat{\boldsymbol{\mathcal{X}}})$, which is a key property ensuring well-posedness.

Let us then denote by $\widehat{\mathcal{X}}=\begin{bmatrix}\widehat{\boldsymbol{\mathcal{X}}}_1 & \widehat{\boldsymbol{\mathcal{X}}}_2\end{bmatrix}$ the matrix gathering the correctors, and by $\widehat{\mathcal{X}}^*=(\widehat{\mathcal{X}}^*_{ij})_{1\le i,j\le 2}$ its average over the unit cell:

$$\widehat{\mathcal{X}}^*_{ij}(x) := \int_Y \mathcal{X}_{ij}(x,y)\,\mathrm{d}y. \tag{B.2}$$

The correctors $(\widehat{\boldsymbol{\mathcal{X}}}_j,\widehat{\alpha}_j)$ are those that naturally come into play when using the method of two scale expansions. They allow us to obtain the following proposition, which turns out to be equivalent to Proposition 3.1 after proving (in Proposition B.2 below) that $\widehat{\mathcal{X}}^*(x)=\mathcal{X}^*(x)$.

**Proposition B.1.** *Let $(\boldsymbol{u}, p)$ be the solution to the following Darcy system:*

$$\begin{cases} \boldsymbol{u}(x) = \widehat{\mathcal{X}}^*(x)(\boldsymbol{f}(x) - \nabla p(x)), & x \in \Phi(D), \\ \operatorname{div}(\boldsymbol{u}(x)) = 0, & x \in \Phi(D), \\ \displaystyle\int_{\Phi(D)} p(x)\,\mathrm{d}x = 0, & \\ \boldsymbol{u},\ p \text{ are } \Phi(D) \text{ periodic.} & \end{cases} \tag{B.3}$$

*The following asymptotic expansion holds for the solution $(\boldsymbol{u}_\epsilon, p_\epsilon)$ to the perforated Stokes system (3.1) in the deformed domain $\Phi(D_\epsilon)$:*

$$\boldsymbol{u}_\epsilon(x) = \epsilon^2 \widehat{\mathcal{X}}(x, \Phi^{-1}(x)/\epsilon)(\boldsymbol{f}(x) - \nabla p(x)) + O(\epsilon^3), \qquad p_\epsilon(x) = p(x) + O(\epsilon), \tag{B.4}$$

*where the error terms are measured with the $L^2$ norm on $\Phi(D_\epsilon)$.*

*Proof.* We only sketch the proof of this result: we detail the derivation of (B.3) and (B.4), but we do not prove in details the estimates $O(\epsilon^3)$ and $O(\epsilon)$ which can be obtained by following the methods outlined in [16, 34].

For deriving the asymptotic (B.4), we apply the method of two scale expansions which postulates the following ansatz:

$$\boldsymbol{u}_\epsilon(x) = \sum_{k=0}^{+\infty} \epsilon^{k+2} \boldsymbol{u}_k(x, \Phi^{-1}(x)/\epsilon), \quad p_\epsilon = \sum_{k=0}^{+\infty} \epsilon^k (p_k^*(x) + \epsilon p_k(x, \Phi^{-1}(x)/\epsilon)), \tag{B.5}$$

where $\boldsymbol{u}_k(x,y)$, $p_k(x,y)$, $p_k^*(x)$ are functions defined for $x \in \Phi(D)$, $y \in Y$, which are $\Phi(D)$ periodic in $x$ and $P$–periodic in $y$. Note that (B.5) are non-standard two-scale periodic expansions owing to the dependence to the deformation of the cell $\Phi^{-1}$ (also considered in [69]). Following [31], we require furthermore the following conditions in order to determine uniquely the functions $p_k^*$ and $p_k(x,y)$:

$$\int_{\Phi(D)} p_k^*(x) = 0\,\mathrm{d}x \text{ and } \int_Y p_k(x,y)\,\mathrm{d}y = 0.$$

Using the chain rule, and assuming the Einstein notation convention on repeated indices, we find:

$$\begin{aligned} -\Delta \boldsymbol{u}_k(x, \Phi^{-1}(x)/\epsilon) &= -\partial_{ii} \boldsymbol{u}_k(x, \Phi^{-1}(x)/\epsilon) = -\partial_i \left( \partial_{x_i} \boldsymbol{u}_k(x, \Phi^{-1}(x)/\epsilon) + \epsilon^{-1} \partial_i \Phi_j^{-1}(x) \partial_{y_j} \boldsymbol{u}_k(x, \Phi^{-1}(x)/\epsilon) \right) \\ &= -\Delta_{xx} \boldsymbol{u}_k(x, \Phi^{-1}(x)/\epsilon) - 2\epsilon^{-1} \partial_i \Phi_j^{-1}(x) \partial_{x_i, y_j} \boldsymbol{u}_k(x, \Phi^{-1}(x)/\epsilon) \\ &\quad - \epsilon^{-1} \partial_{ii} \Phi_j^{-1}(x) \partial_{y_j} \boldsymbol{u}_k(x, \Phi^{-1}(x)/\epsilon) - \epsilon^{-2} \partial_i \Phi_j^{-1}(x) \partial_i \Phi_l^{-1}(x) \partial_{y_j y_l} \boldsymbol{u}_k(x, \Phi^{-1}(x)/\epsilon) \\ &= -(A_{xx} + \epsilon^{-1} A_{xy} + \epsilon^{-2} A_{yy}) \boldsymbol{u}_k(x, \Phi^{-1}(x)/\epsilon), \end{aligned}$$

where $A_{xx}$, $A_{xy}$ and $A_{yy}$ are the following differential operators:

$$\begin{aligned} A_{xx}\boldsymbol{v}(x,y) &:= \Delta_{xx} \boldsymbol{v}(x,y) = \partial_{x_i x_i} \boldsymbol{v}(x,y), \\ A_{xy}\boldsymbol{v}(x,y) &:= 2\partial_i \Phi_j^{-1}(x) \partial_{x_i y_j} \boldsymbol{v}(x,y) + \partial_{ii} \Phi_j^{-1}(x) \partial_{y_j} \boldsymbol{v}(x,y), \\ A_{yy}\boldsymbol{v}(x,y) &:= \partial_i \Phi_j^{-1}(x) \partial_i \Phi_l^{-1}(x) \partial_{y_j y_l} \boldsymbol{v}(x,y) = \operatorname{div}_y(A(x) \nabla_y \boldsymbol{v}(x,y)). \end{aligned}$$

We also have, still by applying the chain rule:

$$\nabla p_k(x, \Phi^{-1}(x)/\epsilon) = \nabla_x p_k(x, \Phi^{-1}(x/\epsilon)) + \epsilon^{-1} (\nabla \Phi^{-1}(x))^T \nabla_y p_k(x, \Phi^{-1}(x)/\epsilon).$$

$$\begin{aligned} \operatorname{div}(\boldsymbol{u}_k(x, \Phi^{-1}(x)/\epsilon)) &= \operatorname{Tr}(\nabla_x \boldsymbol{u}_k + \epsilon^{-1} \nabla_y \boldsymbol{u}_k \nabla \Phi^{-1}) \\ &= \operatorname{div}_x \boldsymbol{u}_k + \epsilon^{-1} \operatorname{div}_y(\nabla \Phi^{-1} \boldsymbol{u}_k). \end{aligned}$$

Therefore, inserting (B.5) into (3.1) yields

$$\begin{aligned} \boldsymbol{f} &= \sum_{k=0}^{+\infty} \left[ -(A_{xx} \epsilon^{k+2} \boldsymbol{u}_k + \epsilon^{k+1} A_{xy} \boldsymbol{u}_k + \epsilon^k A_{yy} \boldsymbol{u}_k) + \epsilon^k \nabla p_k^* + \epsilon^{k+1} \nabla_x p_k + \epsilon^k (\nabla \Phi^{-1})^T \nabla_y p_k \right] \\ &= \sum_{k=0}^{+\infty} \epsilon^k \left[ -A_{xx} \boldsymbol{u}_{k-2} - A_{xy} \boldsymbol{u}_{k-1} - A_{yy} \boldsymbol{u}_k + \nabla p_k^* + \nabla_x p_{k-1} + (\nabla \Phi^{-1})^T \nabla_y p_k \right], \end{aligned} \tag{B.6}$$

and

$$\begin{aligned} 0 &= \sum_{k=0}^{+\infty} \epsilon^{k+2} \operatorname{div}(\boldsymbol{u}_k(\cdot, \Phi^{-1}(\cdot)/\epsilon)) = \sum_{k=0}^{+\infty} \epsilon^{k+2} (\operatorname{div}_x \boldsymbol{u}_k + \epsilon^{-1} \operatorname{div}_y(\nabla \Phi^{-1} \boldsymbol{u}_k)) \\ &= \sum_{k=0}^{+\infty} \epsilon^{k+1} (\operatorname{div}_x \boldsymbol{u}_{k-1} + \operatorname{div}_y((\nabla \Phi^{-1}) \boldsymbol{u}_k)), \end{aligned} \tag{B.7}$$

where we use the convention $\boldsymbol{u}_{-2} = \boldsymbol{u}_{-1} = 0$ and $p_{-1} = p_{-2} = 0$. Let us assume that $\boldsymbol{f}$ is given by a power series in $\epsilon$:

$$\boldsymbol{f}(x) = \sum_{k=0}^{+\infty} \epsilon^k \boldsymbol{f}_k.$$

Identifying identical powers of $\epsilon$ in (B.6) and (B.7), we read the following cascade of equations:

$$\begin{cases} -A_{yy}\boldsymbol{u}_k + (\nabla\Phi^{-1})^T\nabla_y p_k = \boldsymbol{f}_k - \nabla p_k^* - \nabla_x p_{k-1} + A_{xy}\boldsymbol{u}_{k-1} + A_{xx}\boldsymbol{u}_{k-2} & \text{in } \Phi(D)\times Y,\ \forall k\geq 0,\\ \operatorname{div}_y((\nabla\Phi^{-1})\boldsymbol{u}_k) = -\operatorname{div}_x \boldsymbol{u}_{k-1} & \text{in } \Phi(D)\times Y, \forall k\geq 0,\\ \boldsymbol{u}_{-1} = \boldsymbol{u}_{-2} = 0, \quad p_{-1} = 0, & \\ \displaystyle\int_{\Phi(D)} p_k^*(x)\,\mathrm{d}x = 0 & \forall k\geq 0,\\ \displaystyle\int_Y p_k(x,y)\,\mathrm{d}y = 0, & \forall x\in\Phi(D),\quad \forall k\geq 0,\\ \boldsymbol{u}_k(x,\cdot) = 0 & \text{on } \partial Y,\ \forall x\in\Phi(D),\\ \boldsymbol{u}_k(x,\cdot) \text{ is } P\text{–periodic for any } x\in\Phi(D) & \forall k\geq 0,\\ \boldsymbol{u}_k(\cdot,y) \text{ is } \Phi(D)\text{–periodic for any } y\in P & \forall k\geq 0. \end{cases} \tag{B.8}$$

An important difference of (B.8) with respect to the same analysis where $\Phi$ is just the identity mapping lies in the fact that the operator $A_{yy} = \operatorname{div}_y(A(x)\nabla_y\cdot)$ now depends on $x$. However, it is still possible to find solutions to (B.8) decoupling the slow variable $x$ and the fast variable $y \equiv \Phi^{-1}(x)/\epsilon$. For the proof of the present Proposition 3.1, we content ourselves to the first order approximation obtained by identifying the solutions to (B.8) for $k = 0$ and $k = 1$.

For $k = 0$, the system (B.8) reads, for a given fixed $x\in\Phi(D)$:

$$\begin{cases} -\operatorname{div}_y(A(x)\nabla_y\boldsymbol{u}_0(x,y)) + (\nabla\Phi^{-1}(x))^T\nabla_y p_0(x,y) = \boldsymbol{f}_0(x) - \nabla p(x), & \forall y\in Y,\\ \operatorname{div}_y(\nabla\Phi^{-1}(x)\boldsymbol{u}_0(x,y)) = 0 & \forall y\in Y,\\ \boldsymbol{u}_0(x,\cdot) = 0 & \text{on } \partial Y,\\ \boldsymbol{u}_0(x,\cdot) \text{ is } P\text{–periodic.} & \end{cases}$$

This problem has a unique solution $(\boldsymbol{u}_0, p)$ given by

$$\boldsymbol{u}_0(x,y) = \widehat{\boldsymbol{\mathcal{X}}}_j(x,y)(f_{0,j}(x) - \partial_j p(x)), \qquad p_0(x,y) = \widehat{\alpha}_j(x,y)(f_{0,j}(x) - \partial_j p(x)), \tag{B.9}$$

where $(\widehat{\boldsymbol{\mathcal{X}}}_j, \widehat{\alpha}_j)_{1\leq j\leq d}$ are the solution to the cell problem (B.1). It remains to identify the function $p(x)$ in (B.9), which is possible by examining (B.8) with $k = 1$:

$$\begin{cases} -\operatorname{div}_y(A(x)\nabla_y\boldsymbol{u}_1) + (\nabla\Phi^{-1}(x))^T\nabla_y p_1 = \boldsymbol{f}_1 - \nabla p_1^* - \nabla_x p_0 + A_{xy}\boldsymbol{u}_0,\\ \operatorname{div}_y((\nabla\Phi^{-1})\boldsymbol{u}_1) = -\operatorname{div}_x(\boldsymbol{u}_0),\\ \boldsymbol{u}_1(x,\cdot) = 0 \text{ on } \partial Y,\\ \boldsymbol{u}_1(x,\cdot) \text{ is } P\text{–periodic.} \end{cases}$$

By the Fredholm alternative, this elliptic problem has a solution if and only if the following compatibility condition is satisfied:

$$\int_Y \operatorname{div}_x(\boldsymbol{u}_0)\,\mathrm{d}y = 0.$$

This condition can be rewritten

$$0 = \operatorname{div}_x\left(\int_Y \widehat{\boldsymbol{\mathcal{X}}}_j(x,y)(f_{0,j}(x) - \partial_j p_0^*(x))\,\mathrm{d}y\right) = \operatorname{div}(\widehat{\mathcal{X}}^*(x)(\boldsymbol{f} - \nabla p)),$$

which is equivalent to (3.5). This proves that if the expansion (B.5) exists, then the terms $\boldsymbol{u}_0$ and $p$ are solution to the Darcy system (3.5). On this periodic setting, the error bounds (B.4) can then be proven by using standard elliptic estimates, see e.g. [16, 31]. □

The next proposition relates the cell problem (B.1) with non-homogeneous coefficients on the rectangle cell $Y$ to the one (3.2) with constant coefficients but posed on the deformed cell $\nabla\Phi(\Phi^{-1}(x))Y$.

**Proposition B.2.** *The following identity holds for the cell solutions $(\widehat{\boldsymbol{\mathcal{X}}}_j, \widehat{\alpha}_j)$ of (B.1):*

$$\widehat{\boldsymbol{\mathcal{X}}}_j(x,y) := \boldsymbol{\mathcal{X}}_j(x, \nabla\Phi(\Phi^{-1}(x))y), \quad \widehat{\alpha}_j(x,y) := \alpha_j(x, \nabla\Phi(\Phi^{-1}(x))y), \qquad \forall x\in\Phi(D),\ \forall y\in Y. \tag{B.10}$$

*where $(\boldsymbol{\mathcal{X}}_j, \alpha_j)$ is the cell solution to the problem (3.2).*

*Proof.* Let us introduce the auxiliary correctors

$$\widetilde{\boldsymbol{\mathcal{X}}}_j(x,z) := \boldsymbol{\mathcal{X}}_j(x,\nabla\Phi^{-1}(x)z), \quad \widetilde{\alpha}_j(x,z) := \alpha_j(x,\nabla\Phi^{-1}(x)z)$$

defined for any $x \in \Phi(D)$ and $z \in \nabla\Phi(\Phi^{-1}(x))Y$. In virtue of $(\nabla\Phi^{-1}(x))^{-1} = \nabla\Phi(\Phi^{-1}(x))$, the result is proved as soon as we show that $\widetilde{\boldsymbol{\mathcal{X}}}_j = \boldsymbol{\mathcal{X}}_j$ and $\widetilde{\alpha}_j = \alpha_j$. First, it is straightforward to see that both $\boldsymbol{\mathcal{X}}_j(x,\cdot)$ and $\widetilde{\boldsymbol{\mathcal{X}}}_j(x,\cdot)$ satisfy the same boundary conditions on $\nabla\Phi(\Phi^{-1}(x))Y$. Then, the use of the chain rule implies that these functions also satisfy the same differential equations:

$$\begin{aligned}
\Delta_{zz}\widetilde{\boldsymbol{\mathcal{X}}}_j(x,\nabla\Phi^{-1}(x)z) + \nabla_z\widetilde{\alpha}_j(x,\nabla\Phi^{-1}(x)z) &= \partial_{z_iz_i}(\boldsymbol{\mathcal{X}}_j(x,\nabla\Phi^{-1}(x)z)) + \partial_{z_l}\widetilde{\alpha}_j(x,\nabla\Phi^{-1}(x)z)\boldsymbol{e}_l \\
&= \partial_i\Phi_k^{-1}(x)\partial_i\Phi_l^{-1}(x)\partial_{y_k}\partial_{y_l}\boldsymbol{\mathcal{X}}_j(x,\nabla\Phi^{-1}(x)z) + \partial_l\Phi_k^{-1}(x)\partial_{y_k}\widetilde{\alpha}_j(x,\nabla\Phi^{-1}(x)z)\boldsymbol{e}_l \\
&= \left[A_{yy}\widetilde{\boldsymbol{\mathcal{X}}}_j + (\nabla\Phi^{-1}(x))^T\nabla_y\widetilde{\alpha}_j\right](x,\nabla\Phi(\Phi^{-1}(x)z)) \\
&= \boldsymbol{e}_j,
\end{aligned}$$

$$\begin{aligned}
\operatorname{div}_z(\widetilde{\boldsymbol{\mathcal{X}}}_j(x,\nabla\Phi^{-1}(x)z)) &= \operatorname{Tr}(\nabla_z\widetilde{\boldsymbol{\mathcal{X}}}_j(x,\nabla\Phi^{-1}(x)z)) \\
&= \operatorname{Tr}(\nabla_y\widetilde{\boldsymbol{\mathcal{X}}}_j(x,\nabla\Phi^{-1}(x)z)\nabla\Phi^{-1}(x)) \\
&= \operatorname{div}_y((\nabla\Phi^{-1}(x))^T\widetilde{\boldsymbol{\mathcal{X}}}_j(x,\nabla\Phi^{-1}(x)z)) = 0.
\end{aligned}$$

This implies the result by uniqueness of the solutions to the cell problem (3.2). □

Performing the change of variable $y = \nabla\Phi^{-1}(x)z$ in (B.2) and using $\nabla\Phi^{-1}(x) = \nabla\Phi(\Phi^{-1}(x))^{-1}$, we find that the tensors $\mathcal{X}^*$ of (3.4) and $\widehat{\mathcal{X}}^*$ of (B.2) coincide:

$$\begin{aligned}
\widehat{\mathcal{X}}^*(x) &= \int_Y \widehat{\mathcal{X}}(x,y)\,\mathrm{d}y \\
&= |\nabla\Phi^{-1}(x)| \int_{\nabla\Phi(\Phi^{-1}(x))Y} \widehat{\mathcal{X}}(x,\nabla\Phi^{-1}(x)z)\,\mathrm{d}z = \mathcal{X}^*(x).
\end{aligned}$$

This shows the equivalence of the Darcy systems (3.5) and (B.3). Then (3.6) follows from (B.4) together with (B.10). This completes the proof of Proposition 3.1.

### B.2. Proof of Proposition 3.2

Let us recall elementary commutation identities for the Laplace, gradient and divergence operators with respect to rotation and rescaling.

**Lemma B.1.** *Let $s > 0$ and $R \in \mathbb{R}^{2\times 2}$ a rotation matrix satisfying $R^TR = I$. For any vector and scalar fields $\boldsymbol{\mathcal{X}} \in \mathcal{C}^\infty(\mathbb{R}^2,\mathbb{R}^2)$, $\alpha \in \mathcal{C}^\infty(\mathbb{R}^2,\mathbb{R})$, the following identities hold:*

$$\begin{aligned}
\Delta(R^T\boldsymbol{\mathcal{X}}\circ(sR)) &= s^2R^T(\Delta\boldsymbol{\mathcal{X}})\circ(sR), \\
\nabla(\alpha\circ(sR)) &= sR^T(\nabla\alpha)\circ(sR). \\
\operatorname{div}(R^T\boldsymbol{\mathcal{X}}\circ(sR)) &= s\operatorname{div}(\boldsymbol{\mathcal{X}})\circ(sR).
\end{aligned}$$

This lemma implies the following identities relating the solution to the cell problems (3.2) and (3.10) in respectively the rotated and rescaled cell $\nabla\Phi(\Phi^{-1}(x))Y$ to that in the unit cell $Y$.

**Proposition B.3.** *If $\nabla\Phi(\Phi^{-1}(x)) = s(x)R(x)$ with $s(x) > 0$ and $R(x)^TR(x) = I$, then the solution to (3.2) reads*

$$\boldsymbol{\mathcal{X}}_j(x,z) = s^2R_{jl}(x)R(x)\boldsymbol{\mathcal{X}}_l(s^{-1}R(x)^Tz), \qquad \alpha_j(x,z) = sR_{jl}(x)\alpha_l(s^{-1}R(x)^Tz), \tag{B.11}$$

*where $(\boldsymbol{\mathcal{X}}_j(y),\alpha(y)_j)$ are the solutions to the cell problem posed in the perforated unit cell $Y = P\backslash T$:*

$$\begin{cases}
-\Delta_{yy}\boldsymbol{\mathcal{X}}_j + \nabla\alpha_j = \boldsymbol{e}_j \text{ in } P, \\
\operatorname{div}(\boldsymbol{\mathcal{X}}_j) = 0 \text{ in } P, \\
\displaystyle\int_Y \alpha_j(y)\,\mathrm{d}y = 0, \\
\boldsymbol{\mathcal{X}}_j = 0 \text{ on } \partial Y, \\
\boldsymbol{\mathcal{X}}_j \text{ is } P\text{–periodic.}
\end{cases}$$

*Proof.* By applying Lemma B.1, we find

$$\begin{aligned}
\Delta_{zz}\boldsymbol{\mathcal{X}}_j(x,\cdot) + \nabla_z\alpha_j(x,\cdot) &= R_{jl}(x)\left(\Delta_{zz}(s^2R(x)\boldsymbol{\mathcal{X}}_l\circ(s^{-1}R(x)^T)) + \nabla_z(s\alpha_l\circ(s^{-1}R(x)^T))\right) \\
&= R_{jl}(x)\left(R(x)(\Delta_{yy}\widetilde{\boldsymbol{\mathcal{X}}}_l + \nabla_{yy}\widetilde{\alpha}_l)\circ(s^{-1}R(x)^T)\right) = R_{jl}(x)R(x)\boldsymbol{e}_l \\
&= R(x)R(x)^T\boldsymbol{e}_j = \boldsymbol{e}_j,
\end{aligned}$$

and

$$\mathrm{div}_z(\boldsymbol{\mathcal{X}}_j(x,\cdot)) = \mathrm{div}(s^2 R_{lj}(x) R(x) \boldsymbol{\mathcal{X}}_l \circ (s^{-1} R(x)^T)) = 0.$$

Since $s^2 R_{jl}(x) R(x) \boldsymbol{\mathcal{X}}_l(s^{-1} R(x)^T \cdot)$ also satisfies the boundary conditions of (3.2) on $\nabla\Phi(\Phi^{-1}(x))Y = s(x)R(x)Y$, we obtain the result. □

The proof of Proposition 3.2 follows by the change of variable $y = s^{-1} R(x)^T z$ in the formula (3.4):

$$\begin{aligned}
\mathcal{X}^*_{ij}(x) &= \frac{1}{|s(x)R(x)P|} \int_{s(x)R(x)Y} \boldsymbol{e}_i^T \boldsymbol{\mathcal{X}}_j(x,z)\,\mathrm{d}z \\
&= s(x)^{-2} \int_{s(x)R(x)Y} s(x)^2 R_{jl} \boldsymbol{e}_i^T R \boldsymbol{\mathcal{X}}_l(s^{-1} R^T z)\,\mathrm{d}z \\
&= s(x)^2 R_{jl} R_{ik} \int_Y \boldsymbol{e}_k^T \boldsymbol{\mathcal{X}}_l(z)\,\mathrm{d}z = s(x)^2 R_{jl} R_{ik} \mathcal{X}^*_{kl} = s(x)^2 R(x) \mathcal{X}^* R(x)^T.
\end{aligned}$$